

Review

# Review on the Tensile Properties and Strengthening Mechanisms of Additive Manufactured CoCrFeNi-Based High-Entropy Alloys

Zhining Wu <sup>1,2,3</sup>, Shanshan Wang <sup>1,2</sup>, Yunfeng Jia <sup>1,2</sup>, Weijian Zhang <sup>1,2</sup>, Ruiguang Chen <sup>1,2</sup>, Boxuan Cao <sup>2,\*</sup>, Suzhu Yu <sup>1,2,\*</sup>  and Jun Wei <sup>1,2,4,\*</sup>

<sup>1</sup> Shenzhen Key Laboratory of Flexible Printed Electronics Technology, Harbin Institute of Technology (Shenzhen), Shenzhen 518055, China

<sup>2</sup> School of Materials Science and Engineering, Harbin Institute of Technology (Shenzhen), Shenzhen 518055, China

<sup>3</sup> School of Mechanical and Automotive Engineering, Ningbo University of Technology, Ningbo 315211, China

<sup>4</sup> State Key Laboratory of Advanced Welding and Joining, Harbin Institute of Technology, Harbin 150001, China

\* Correspondence: caoboxuan@hit.edu.cn (B.C.); szyu@hit.edu.cn (S.Y.); junwei@hit.edu.cn (J.W.)

**Abstract:** The advent of high-entropy alloys (HEAs) provides new possibilities for the metallurgical community. CoCrFeNi-based alloys have been widely recognized to demonstrate superior mechanical properties, amongst the high-entropy alloy systems; in particular, they possess an outstanding tensile ductility and work-hardening capacity. Additive manufacturing (AM) uses a layer-by-layer material deposition approach to build parts directly from computer-aided design models, which are capable of producing near-net-shape HEAs with superior mechanical properties, surpassing traditional manufacturing methods that require a time-consuming post-treatment process, such as cutting, milling, and molding. Moreover, the rapid solidification inherent in AM processes induces the formation of high-density dislocations, which are capable of enhancing the mechanical properties of HEAs. This review comprehensively investigates and summarizes the diverse strengthening mechanisms within CoCrFeNi-based alloys produced using AM technologies, with a specific focus on their influence on tensile properties. A correlation is established between the AM processing parameters and the resultant phases and microstructures, as well as the mechanical properties of CoCrFeNi-based HEAs, which provide guidelines to achieve a superior strength–ductility synergy.

**Keywords:** high-entropy alloy; additive manufacturing; strengthening mechanisms; CoCrFeNi-based alloys; tensile properties



**Citation:** Wu, Z.; Wang, S.; Jia, Y.; Zhang, W.; Chen, R.; Cao, B.; Yu, S.; Wei, J. Review on the Tensile Properties and Strengthening Mechanisms of Additive Manufactured CoCrFeNi-Based High-Entropy Alloys. *Metals* **2024**, *14*, 437. <https://doi.org/10.3390/met14040437>

Academic Editor: Andrea Di Schino

Received: 6 March 2024

Revised: 29 March 2024

Accepted: 4 April 2024

Published: 9 April 2024



**Copyright:** © 2024 by the authors. Licensee MDPI, Basel, Switzerland. This article is an open access article distributed under the terms and conditions of the Creative Commons Attribution (CC BY) license (<https://creativecommons.org/licenses/by/4.0/>).

## 1. Introduction

Metallic materials have been indispensable throughout human history. For example, the discovery and use of bronze, an alloy made of copper and tin, helped humankind enter the Bronze Age from the primitive Stone Age. Due to significant advancements in science and engineering, the limitations of metallic materials' properties have been consistently worked upon and broken down. Therefore, humans persistently endeavor to investigate uncharted territories inside the phase map to discover high-performance alloys. As reported by Yeh [1] and Cantor [2] in 2004, a new alloy design strategy was raised to explore the alloying space in the center of the phase diagram. These sorts of new metallic materials are known as high-entropy alloys (HEAs). In contrast with traditional alloys, HEAs are usually composed of several principal components in equal or approximately equal proportions, without a dominant component. The four core effects of HEAs, including the high-entropy effect, sluggish diffusion effect, lattice distortion effect, and cocktail effect, contribute to the alloy's high strength, high hardness, and remarkable irradiation stability [3–12].

Among a vast number of HEA materials, CoCrFeNi-based alloys have attracted significant research attention and have been extensively investigated due to their excellent mechanical properties, especially their unique strength–ductility synergy at cryogenic

temperatures. Because the enthalpy of mixing between the transition elements of Co, Cr, Fe, and Ni is small and their atomic sizes are comparable, CoCrFeNi-based alloys are more likely to form a solid solution phase. One of the earliest known HEAs was the quinary CrMnFeCoNi alloy, also referred to as the cantor alloy [2]. The literature demonstrates that the cantor alloy has outstanding cryogenic strength [13], hardness [14], and ductility [15]. The dislocation structure and the evolution of the microstructure under various strains have the most significant effects on the mechanical characteristics. As strain and temperature decrease, the deformation mode shifts from dislocation slip, caused by the planar glide of  $\langle 110 \rangle$  dislocations on  $\{111\}$  planes, to twinning [13,16]. The deformation twin, surrounded by the stacking faults, can be observed and increased with the strain due to the low stacking fault energy (SFE) of the cantor alloy [17]. The essential strain for twinning drops from 24.5% at ambient temperature to 11% at cryogenic temperature, along with an elevated work hardening rate [18]. Twin boundaries have the ability to effectively impede dislocation motion and enhance the cantor alloy's strength and ductility. Another representative CoCrFeNi-based alloy is the CoCrFeNiAl<sub>x</sub> alloy. When the content of Al rises, the phase transitions from face-centered cubic (FCC) to body-centered cubic (BCC). By adjusting the amount of the phase fraction, the AlCoCrFeNi HEA's strength and plasticity can be tailored. The plasticity and toughness can be attributed to the presence of the FCC phase, while the strength can be enhanced by the spinodal decomposition structure, which is composed of the B2 and BCC phases. Through the blocking of dislocation movement and the storage of dislocations, the eutectic structure that combines the FCC and BCC/B2 phases can simultaneously enhance the strength and ductility [19].

Stacking-fault energy (SFE) is an important parameter controlling the mechanical properties and underlying deformation mechanisms, particularly among FCC-structured alloys. The introduction of stacking faults in FCC alloys modifies the atomic stacking sequence in the direction of the specified plane, which can be characterized as the intrinsic and extrinsic fault, hexagonal close-packed (HCP) structure, and twinning [20]. The deformation mechanism shifts from dislocation slip to twinning-induced plasticity and transformation-induced plasticity, as the SFE decreases [21–24]. Various deformation substructures can be identified as a result of the complex stacking fault–dislocation–twinning interactions [25]. Such dislocation-related interactions promote dislocation proliferations and contribute to an enhanced strain-hardening capability. Apart from tailoring SFE values and associated deformation mechanisms, there are another two approaches for achieving property enhancement [26–31]. The first one is to dope other elements to the CoCrFeNi matrix to establish a solid solution strengthening and/or an interstitial strengthening mechanism. The second method involves introducing nanoparticles to the CoCrFeNi-based matrix to form a precipitation-strengthening structure.

Recently, with the emergence and development of additive manufacturing (AM) processes, there has been a breakthrough in the selection of the alloying element of HEAs. Additive manufacturing, or 3D printing, is a sophisticated manufacturing technique that constructs components layer-by-layer, using liquid, sheet material, or powder raw materials. There are several advantages associated with AM technology over traditional subtractive manufacturing methods [32–34]. Firstly, AM allows the design and production of parts without shape constraints. Secondly, AM is a rapidly evolving manufacturing process, offering a greatly reduced time-to-market. Thirdly, AM exhibits little wastage and has a high material utilization rate. Lastly, AM demonstrates a good process repeatability, ensuring consistent and reliable production outcomes. All these advantages make AM a competitive manufacturing method for a wide range of applications.

Powder bed fusion (PBF) is one of the most popular manufacturing methods for HEAs among all the AM processes and it can be divided into two processes, according to the input energy sources—laser powder bed fusion (LPBF) and electron beam melting (EBM). Directed energy deposition (DED) is another effective AM process to process HEA materials. The main difference between the PBF and DED is the way in which the powder is deposited and processed; the powder is sprayed concurrently with the input energy source

through a coaxial nozzle during the DED process instead of being pre-deposited on the substrate, as in the PBF process. The two most utilized techniques in DED for HEAs, with different energy sources, are laser-directed energy deposition (LDED) and powder plasma arc additive manufacturing (PPA-AM). The parts manufactured by either PBF or DED processes are subjected to a rapid cooling rate within a small melt pool, resulting in grain refinement and large residual stress. High strength or even an extraordinary combination of strength–ductility can generally be achieved by comparing it with the counterparts fabricated using conventional processes.

Therefore, the extra strengthening contribution for CoCrFeNi-based alloys is inherent in the design concept of HEAs and the rapid prototyping process. There are already some literature reviews regarding the conception of HEAs [35], 3D-printed HEAs [36], and the mechanical behavior of HEAs [37]. Here, we aim at providing an insightful view towards the composition–processing–structure–properties relationships in HEAs prepared using additive manufacturing. This review will present and discuss the typical methods used to design AMed CoCrFeNi-based alloys. In the present review, various research on improving the mechanical properties within CoCrFeNi-based alloy systems is reviewed. The relationship of tensile properties to manufacturing processes, microstructure, strengthening mechanisms, and deformation mechanisms are systematically discussed and summarized to promote the understanding and guidance of the mechanical response among multicomponent alloy systems.

## 2. Additive Manufacturing of CoCrFeNi-Based Alloys

More and more research is focusing on the use of AM techniques, mainly using PBF and DED techniques, to fabricate CoCrFeNi-based alloys and an increased enhancement of the strength of the CoCrFeNi-based alloys has been demonstrated by numerous studies [38–44]. This improvement can be attributed to the rapid heating and cooling rate involved in the fabrication process, which effectively mitigates element segregation within the samples and induces significant dislocations [45–47]. Figure 1 illustrates a flow chart of additively manufactured (AMed) HEAs and the correlation between the mechanical properties and processing parameters. The constitution of HEAs can be designed and tuned using pre-alloyed powder or a mixture of different elements during production process. The manipulation of processing parameters and subsequent post-treatment procedures significantly influences not only the microstructural characteristics of the samples, but also the mechanical properties and underlying strengthening mechanisms. This section provides an overview of the various phases and crystal characteristics shown by the AMed CoCrFeNi-based alloy.

### 2.1. Powder Bed Fusion

#### 2.1.1. Laser Powder Bed Fusion

LPBF, also referred to as selective laser melting, is one of the most commonly used AM techniques to fabricate metal alloy parts [48,49]. The powder is pre-fed on the platform by a re-coater and the laser scans on the powder bed following a predetermined route from a CAD model. With the movement of the focal point of the laser, the powder is selectively melted and rapidly solidified. The platform drops with a specific distance once the scanning of the current layer is finished. The part is built using a layer-by-layer method, with selected processing parameters such as laser power ( $P$ ), scanning speed ( $v$ ), hatch distance ( $h$ ), and layer thickness ( $L$ ). Prior to conducting any performance evaluations, it is essential to prioritize the determination of the relative density of the AMed HEAs. In order to attain the highest relative density, it is important to adjust the process parameters. The presence of any defects, such as holes and cracks, significantly impacts the mechanical strength of the sample. The processing parameters significantly affect the relative density of the as-built specimen in the following ways: insufficient melting of the powder leads to void formation and the balling effect due to the excessive energy input [50]. Moreover, the

phase composition of prototypes can differ from the raw materials as a result of the rapid heating–cooling cycle and element segregation [51,52].

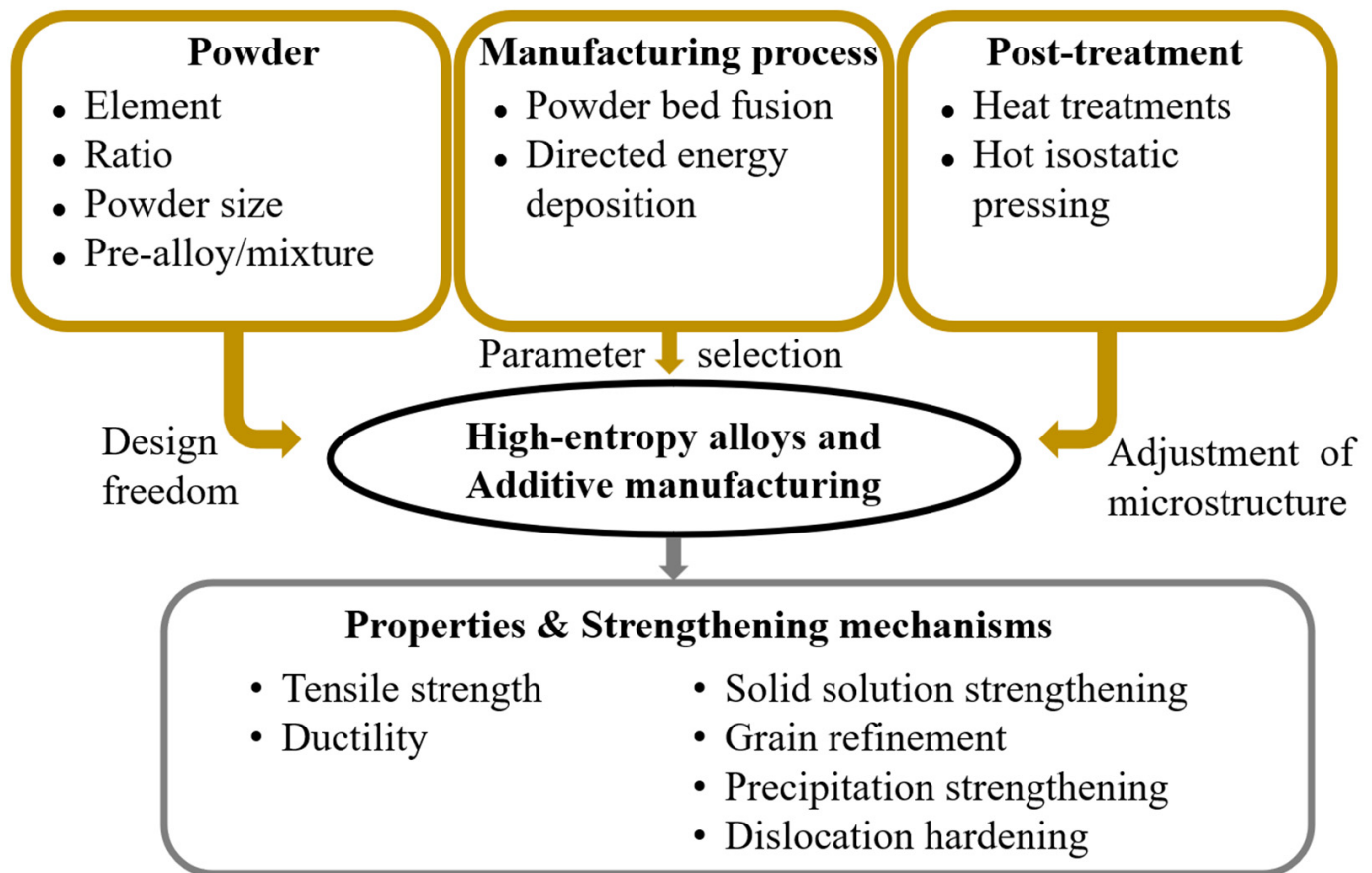


**Figure 1.** Key factors in determining the mechanical properties in AMed HEAs.

The volume energy density (VED, which can be expressed as  $\frac{P}{v \cdot hL}$  [44]) is commonly used to evaluate the input energy. According to Chen et al. [38], it was observed that the density of the bulk CoCrFeNi and CoCrFeNiMn materials exhibited an increase when the input volume energy density was raised. However, after the volume energy density was above a threshold value, the density decreased with further elevated energy density (Figure 2a). Moreover, the high temperature brought about by the input high laser energy leads to the rapid evaporation of the Mn element, due to the low heat of vaporization and the low boiling temperature, which leads to a compositional difference between the as-built component and the raw metal powder (Figure 2b). The distribution of elements is decided by the shape of the melt pool and the remelting phenomenon caused by adjacent scan tracks (Figure 2c,d). In LPBF-prepared (LPBFed) AlCoCrFeNi HEAs, both A2 and ordered B2 phases can be found in the matrix. However, the volume fraction of the two phases can be slightly different when the VED is increased, because the higher cooling rate brought about by the higher VED facilitated the generation of the B2 phase. As seen in Figure 3a–d, more B2 phases can be found in the HEA's A2 phase, as the VED increased [39]. Other examples of the relative density and phase composition of CoCrFeNi-based HEAs manufactured using LPBF are summarized in Table 1.

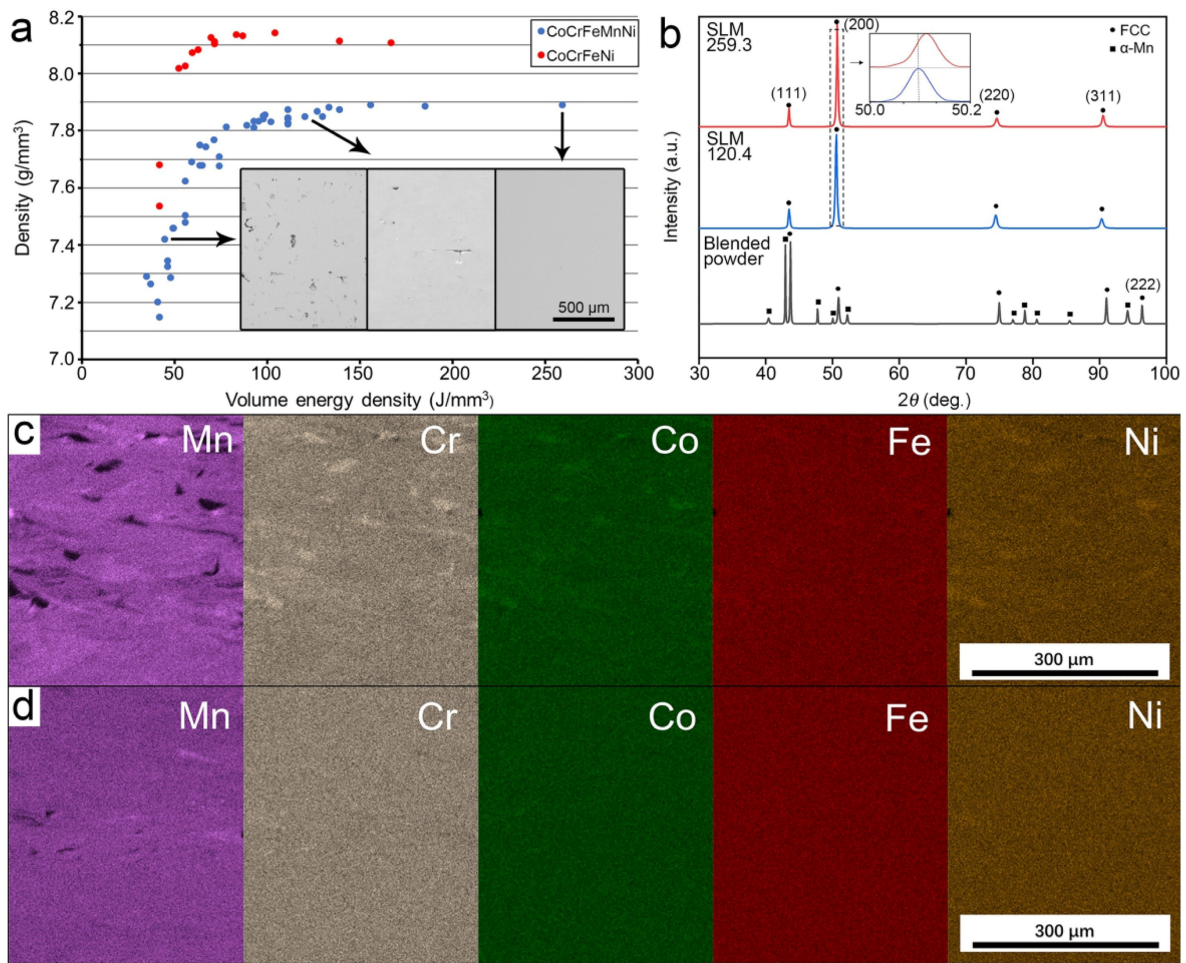


**Figure 2.** (a) The density of an as-built sample of CoCrFeNi and CoCrFeMnNi HEAs changes with the volume energy density. A higher density can be reached with increasing volume energy density. (b) The XRD pattern of blended CoCrFeNi powder and Mn powder before manufacturing and the as-built sample manufactured by varying laser parameters. EDS mapping of (c) samples with larger energy input and (d) samples with smaller energy input, adapted with permission from Ref. [38]. Copyright of © 2024 Elsevier.

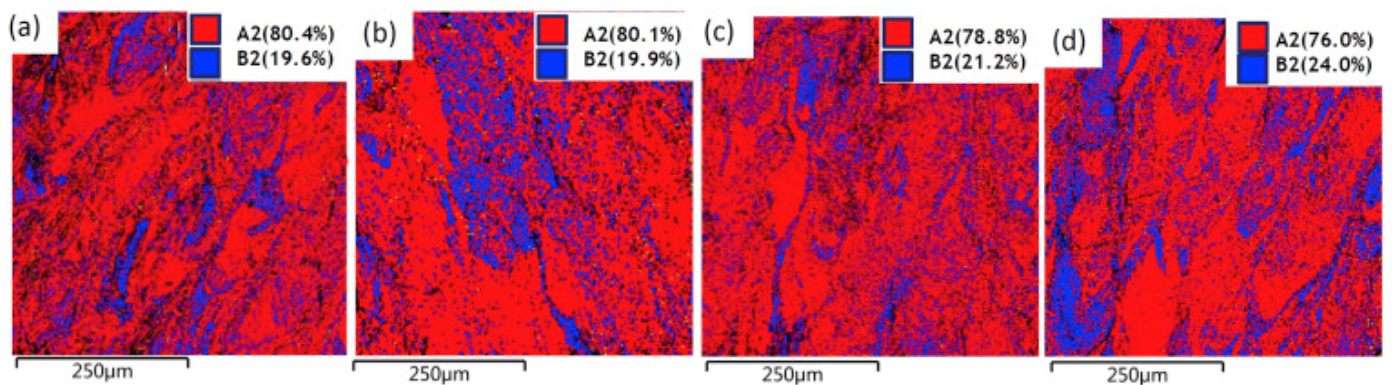


**Figure 3.** The phase fraction evolution among AlCoCrFeNi HEAs manufactured with VED of (a) 68.4 J/mm<sup>3</sup>; (b) 83.3 J/mm<sup>3</sup>; (c) 97.2 J/mm<sup>3</sup>; and (d) 111.1 J/mm<sup>3</sup>, adapted with permission from Ref. [39]. Copyright of © 2024 Elsevier.

**Table 1.** Summary of processing parameters, relative density, and corresponding phases changes for LPBFed CoCrFeNi-based HEAs.

HEA	Apparatus	Processing Parameter	Optimal Relative Density	Phase		Ref.
				Powder	As-Built	
Al <sub>0.1</sub> CoCrFeNi, Al <sub>0.5</sub> CoCrFeNi and Al <sub>1.0</sub> CoCrFeNi	SLM 250 HL	P = 150 W; v = 270 mm/s; h = 100 μm; L = 50 μm	-	-	FCC + BCC (present within alloy 0.5Al and 1.0Al)	[53]
Al <sub>0.3</sub> CoCrFeNi	PROX DMP 200	P = 150–170 W; v = 1100–1300 mm/s; h = 60–80 μm; L = 50 μm	99.9%	-	FCC	[54]
Al <sub>0.5</sub> CoCrFeNi	-	P = 160–320 W; v = 400–2000 mm/s; h = 45 μm; L = 25–30 μm	99.92%	-	FCC + BCC	[55]
AlCoCrFeNi	Concept Laser Mlab	P = 98 W; v = 2000 mm/s; h = 52 μm	-	-	B <sub>2</sub> + BCC	[56]
AlCoCrFeNi <sub>2.1</sub>	EOS M290	P = 350–370 W; v = 950–1000 mm/s; h = 80–100 μm; L = 40 μm	>99.5%	-	FCC + BCC	[40]
AlCoCrFeNi <sub>2.1</sub>	NCL-M2150T	P = 240 W; v = 900 mm/s; h = 70 μm; L = 30 μm	-	FCC + BCC	FCC + BCC	[57]
Al <sub>0.5</sub> FeCoCrNi	Farsoon FS271 M	P = 400 W; v = 1600 mm/s; h = 90 μm; L = 40 μm	-	FCC + BCC	FCC	[58]
CoCrFeMnNi	Concept Laser M2	P = 110–280 W; v = 800–2000 mm/s; h = 45–50 μm; L = 30 μm	-	FCC for CoCrFeNi α -Mn for Mn	FCC	[38]
CoCrFeNiMn	Prox 300	P = 240 W; v = 2000 mm/s; L = 40 μm	99.2%	-	-	[43]
CoCrFeMnNi	SLM125HL	P = 150–300 W; v = 600–1000 mm/s; h = 60/100 μm	-	-	-	[59]
CoCrFeMnNi	Farsoon FS271 M	P = 400 W; v = 800–4000 mm/s; h = 90 μm; L = 30 μm	98.2%	FCC	FCC	[60]
CoCrFeMnNi	LPBF solutions 280 HL	P = 160 W; v = 800 mm/s; h = 50 μm; L = 30 μm	>99.2%	-	-	[61]
Co <sub>1.5</sub> CrFeNi <sub>1.5</sub> Ti <sub>0.5</sub> Mo <sub>0.1</sub>	EOSINT M280	P = 160–270 W; v = 540–1350 mm/s; h = 80–120 μm; L = 40 μm	>99.3%	-	FCC + SC	[62]
FeCoCrNiMn/Fe-based metallic glasses	HUSTBMG-I	P = 185 W; v = 600 mm/s; h = 100 μm; L = 40 μm	-	-	Two different FCC + amorphous phases	[63]
1.8 at% N/FeCoNiCr	FS271M	P = 400 W; v = 1200 mm/s; L = 30 μm	-	-	FCC	[64]
0.2 wt.% C/CoCrFeMnNi	Concept Laser M. Lab	P = 90 W; v = 200 mm/s; h = 80 μm; L = 25 μm	-	-	FCC + Cr <sub>23</sub> C <sub>6</sub> + MnO + MnS	[65]
1 wt.% TiC/CoCrFeMnNi	LPBF-100	P = 160 W; v = 400–1000 mm/s; h = 50 μm; L = 30 μm	>99.4%	-	FCC	[66]
2 wt.% TiC/CoCrFeMnNi	LPBF solutions 280 HL	P = 160 W; v = 800 mm/s; h = 50 μm; L = 30 μm	>99.6%	-	matrix + TiC	[61]
5 wt.% TiN/CoCrFeNiMn	Beijing Yibo 3D Technology YBRP-150	P = 200 W; v = 200–1200 mm/s; h = 80–100 μm; L = 40 μm	>99%	-	FCC + TiN	[67]
12 wt.% TiN/CoCrFeNiMn	-	P = 250 W; v = 450 mm/s; h = 75 μm; L = 45 μm	-	-	FCC + TiN	[68]
(CoCrFeMnNi) <sub>99</sub> C <sub>1</sub>	Concept Laser Mlab	P = 90 W; v = 200/600 mm/s; h = 80 μm; L = 25 μm	-	-	FCC	[59]
CoCrFeNiC <sub>0.05</sub>	Farsoon FS271M	P = 400 W; v = 800 mm/s	-	-	FCC	[41]
CoCrFeNiMn	ProX 300	P = 160–290 W; v = 1500–2500 mm/s; h = 50 μm; L = 40 μm	99.2%	-	FCC	[44]
CoCrFeNiTiMo	-	P = 100–400 W; v = 200–800 mm/s; h = 120 μm; L = 50 μm	99.8%	SC + FCC	SC + FCC	[69]
FeCoCrNiC <sub>0.05</sub>	Farsoon FS271 M	P = 200–400 W; v = 800–2000 mm/s	99%	FCC	FCC	[42]
FeCoCrNiC <sub>0.05</sub>	Farsoon FS271 M	P = 400 W; v = 800 mm/s	-	-	FCC	[70]

SC: simple cubic.

### 2.1.2. Electron Beam Melting

The operating principle of EBM is similar to that of LPBF, except for the electron beam being used as the energy source to melt the metal powder. A vacuum atmosphere is created with a working pressure of about  $10^{-3}$  Pa, which can provide a contamination-free environment during the manufacturing process [71]. The powder size used for EBM (45–105  $\mu\text{m}$ ) is usually larger than that used for LPBF (15–53  $\mu\text{m}$ ). The layer thickness is consequently larger, which leads to a higher efficiency but a low surface quality. Preheating is another distinctive feature of the EBM process. It helps to remove the residual stress from the part, which reduces the tendency for warping and delaminating in the manufacturing process [72]. The smaller temperature gradient in EBM makes the part more ductile with less strength than the LPBFed samples due to the coarser grain size in the same alloy system [73,74]. The involved processing parameters contributing to the quality and properties of the specimens are preheating temperature (T), beam current (I), scanning speed (v), layer thickness (L), and line offset (d).

The research among the AMed HEAs via EBM is relatively limited compared with LPBF. First, the EBM equipment requires a vacuum system, so the cost is higher than that of LPBF. Second, the relative density of the EBMed HEAs is difficult to control. Pores and cracks have frequently been found in EBMed CoCrFeNi-based samples [75–79]. In addition to processing parameters, the quality of feedstock also dramatically impacts the formation of defects in the EBMed sample. Wang et al. [80] found that although the lack of fusion pores is the main reason for the sharp increase in the porosity of the as-built CoCrFeNiMn, the entrapped gas pore existing in the powder also has an adverse effect on the porosity of the sample. Upon gas atomization, the molten metal was impacted by a high-speed atomization gas jet and the gas inside the molten metal might not be able to escape and become trapped in the metal powder, since the solidification of the metal was too fast, leading to the gas pore being inside the powder [80]. The pores originating from the feedstock ranged from 0.42% to 1.19% and are smaller than the lack of fusion pores, as shown in Figure 4. The relative density was in the range of 96.3% to 98.2% and it can reach 99.4% with the optimization of processing parameters. The EBMed parts' microstructure also differs from those manufactured using conventional processes. Fujieda's [75] and Shiratori's [76] studies found that in addition to B2/BCC phases, FCC phases were generated in EBMed AlCoCrFeNi samples, which were not found in as-cast samples or even in raw material powders. The reason for the formation of the FCC phase is that the FCC phase is thermodynamically stable at the preheating temperature of EBM (950 °C). Element fluctuations were analyzed on both a micro and nanoscale. The segregation of Fe and Cr can be observed at the grain boundary in both casted and EBMed samples, as shown in Figure 5b. Furthermore, Fe and Cr segregations can be found inside the sub-grain boundaries in the EBM sample. At the nanoscale, a basket-weave morphology is observed, as illustrated in Figure 5d, which consists of zone A (rich in Al and Ni) and zone B (rich in Cr and Fe). Other examples of relative densities and phase compositions of CoCrFeNi-based HEAs manufactured using EBM are summarized in Table 2.

### 2.2. Directed Energy Deposition

The feedstock of DED is usually powder, although, sometimes, wire can be used as the raw material, depending on the machine. Possible energy sources include lasers and plasma arcs. The DED is also referred to as powder plasma arc additive manufacturing (PPA-AM), wire arc additive manufacturing (WAAM), direct laser fabrication (DLF), direct laser deposition (DLD), laser-melted deposition (LMD), etc. The term DED is uniformly used in this review for clarity. The raw materials are fed through the nozzle and the input energy is activated simultaneously, usually surrounded by a shielding gas. The input energy's focal point and raw materials' flow are aligned on the surface of the deposition. The deposition head moves with the specific track to form the specimens and the quality of the specimens is strongly affected by the input energy/current (P), scanning speed (v), layer thickness (L), hatch space (h), and powder flow rate (u).

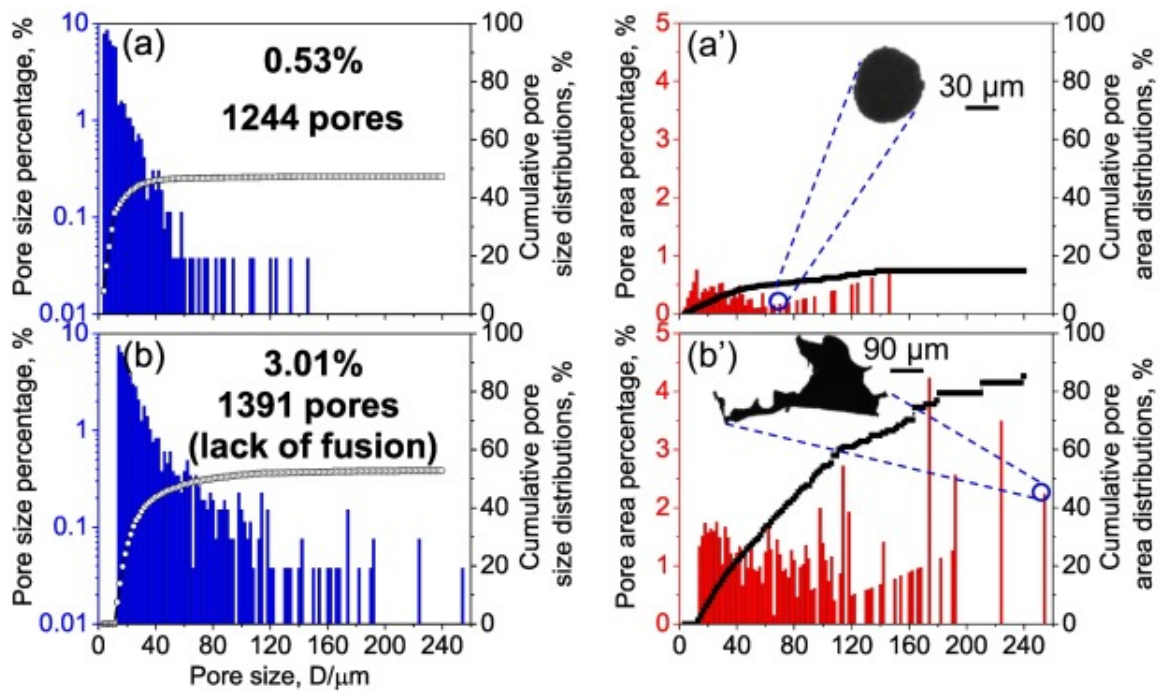


Figure 4. The size and area distribution of (a,a') the gas pores and (b,b') the lack of fusion pores in the EBMed CoCrFeNiMn, adapted with permission from Ref. [80]. Copyright of © 2024 Elsevier.

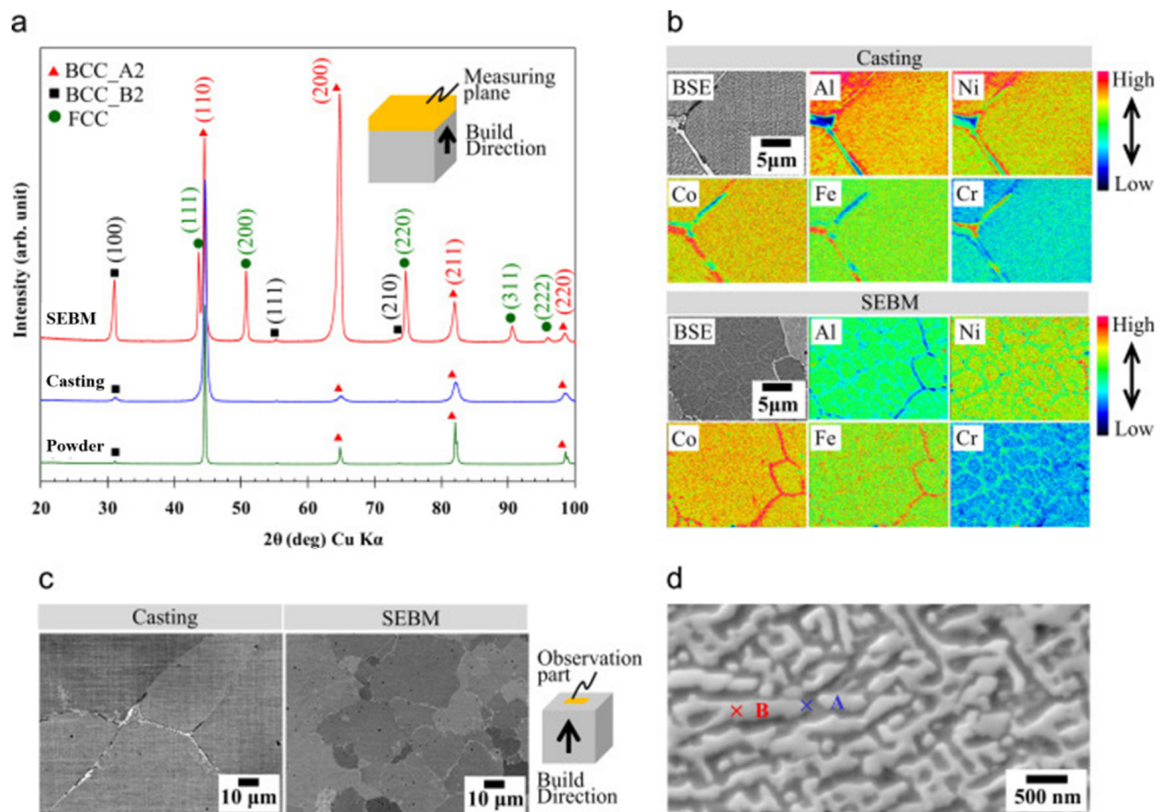
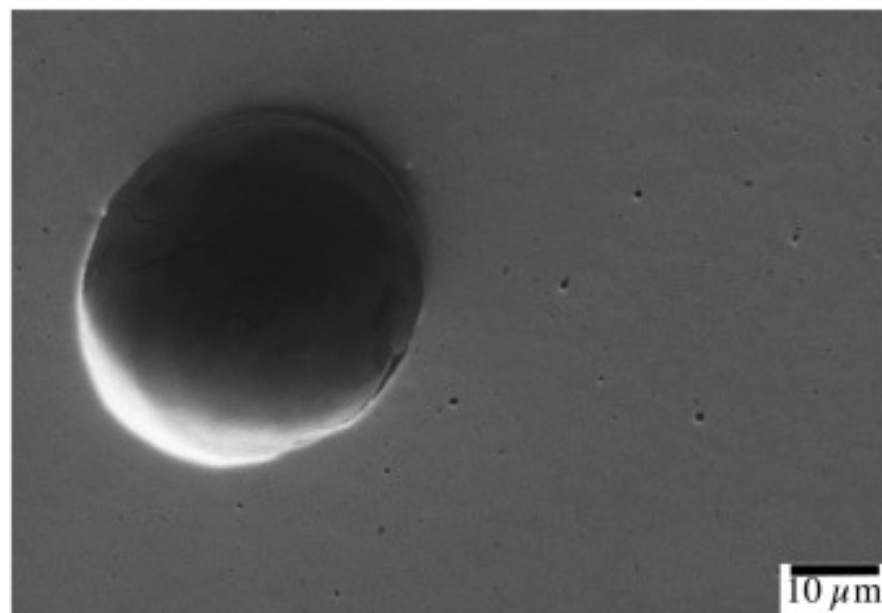


Figure 5. (a) X-ray diffraction patterns of EBMed AlCoCrFeNi alloy, casting AlCoCrFeNi alloy, and powder used for EBM. (b) Backscattered electron (BSE) micrographs of the casting and EBM HEAs. (c) BSE micrographs with higher magnification. (d) Phase separation in SEBM specimen, adapted with permission from Ref. [75]. Copyright of © 2024 Elsevier.

**Table 2.** Summary of processing parameters, relative density, and corresponding phase changes for EBMed CoCrFeNi-based HEAs.

HEA	Apparatus	Processing Parameter	Optimal Relative Density	Phase		Ref.
				Powder	As-Built	
AlCoCrFeNi	Arcam A2X	L = 70 $\mu\text{m}$ ; T = 1173–1233 K	-	BCC	BCC + FCC	[75]
AlCoCrFeNi	Arcam A2X	I = 4.5–9 mA; v = 215 mm/s; d = 260 $\mu\text{m}$ ; L = 70 $\mu\text{m}$ ; T = 1223 K	-	-	FCC + BCC + B2	[76]
AlCoCrFeNi	Arcam A2X	L = 70 $\mu\text{m}$ ; T = 1173–1223 K	-	-	FCC + BCC + B2	[78]
AlCoCrFeNi	Arcam A2X	I = 4.5–9 mA; v = 215 mm/s; d = 260 $\mu\text{m}$ ; L = 70 $\mu\text{m}$ ; T = 1223 K	-	-	FCC + BCC + B2	[81]
Co <sub>1.5</sub> CrFeNi <sub>1.5</sub> Ti <sub>0.5</sub> Mo <sub>0.1</sub>	Arcam A2X	L = 70 $\mu\text{m}$ ; T = 1173–1253 K	-	-	SC/FCC + Ni <sub>3</sub> Ti (disappeared using solution treatment)	[77]
CoCrFeNiMn	-	I = 2–14 mA; v = 492–3446 mm/s; d = 50–150 $\mu\text{m}$ ; L = 50–70 $\mu\text{m}$ ; T = 1173–1253 K	99%	FCC	FCC	[80]

Compared with LPBF and EBM, DED is capable of producing large-sized parts, but its resolution is relatively low [82]. Generally, the relative density of DED samples is highly affected by processing parameters and the quality of the raw material powder. CoCrFeNiMn is one of the most popular alloys in DED prepared (DEDed) CoCrFeNi-based HEAs research. The pores in the DEDed CoCrFeNiMn sample are approximately 30  $\mu\text{m}$  in diameter, as shown in Figure 6 [83]. This type of pore increased the porosity of the DEDed sample to 1.2%. Pores with such a size are mainly created due to the internal pores being filled with atomization gas in the raw material powder. Since elemental powder or pre-alloyed powder is used as the raw material, the resulting phases in the samples can differ due to the change in processing parameters. The FCC phase has been found in most studies [84–87]. However, the BCC phase has also been occasionally identified at the grain boundary of the FCC matrix for the DEDed CoCrFeNiMn sample, and the grain boundary wetting phase transformations governing the secondary phase provide a brief explanation for the grain boundary (GB) phase formation [88]. Table 3 summarizes the DED processing parameters and formed phases for DEDed CoCrFeNi-based alloys.

**Figure 6.** Gas pore and oxides (small black dots) in DEDed CoCrFeMnNi sample, adapted with permission from Ref. [83]. Copyright of © 2024 Elsevier.

**Table 3.** Summary of the processing parameters and constitute phases for DEDed CoCrFeNi-based HEAs.

HEA	Apparatus	Energy Source		Processing Parameters	Phases	Ref.
AlCoCrFeNi		-	Laser	P = 600–650 W; v = 5 mm/s; L = 0.7–0.8 mm	BCC	[46]
AlCoCrFeNi		TRUMPF TruLaser Cell 7040	Laser	P = 800 W; v = 800 mm/min; L = 0.25 mm;	FCC + BCC	[89]
AlCoCrFeNi		LENS MR7	Laser	v = 2.5–40 mm/s; L = 0.15 mm;	B2	[90]
AlCoCrFeNi <sub>2.1</sub>		optomec MR7	Laser	P = 900 W; v = 900 mm/min; u = 30 g/min	BCC + L1 <sub>2</sub>	[91]
AlCoCrFeNi <sub>2.1</sub>		DML-V03AD	Plasma arc	v = 5 mm/s; P = 80 A	FCC + B2 + sigma phase	[92]
Al <sub>0.3</sub> CoCrFeNi		LENS-750	Laser	P = 300 W; v = 170 mm/s; h = 0.381 mm; L = 0.254 mm	FCC + L1 <sub>2</sub>	[93]
Al <sub>0.3</sub> Ti <sub>0.2</sub> Co <sub>0.7</sub> CrFeNi <sub>1.7</sub>		Optomec LENS-750	Laser	P = 300 W; v = 12.7 mm/s; h = 0.381 mm;	FCC + L1 <sub>2</sub>	[94]
Al <sub>x</sub> CoCrFeNi (x = 0.3, 0.6 and 0.85)		TRUMPF TruLaser Cell 7040	Laser	P = 800 W; v = 800 mm/min; L = 0.25 mm; h = 2.6 mm	FCC (x = 0.3); FCC + BCC (x = 0.6); BCC + σ phase (x = 0.85)	[95]
CoCrFeMnNi		-	Laser	P = 370 W; v = 800 mm/min; u = 2 g/min	FCC	[84]
CoCrFeMnNi		-	Laser	P = 300 W; v = 600 mm/min	FCC + BCC	[96]
CoCrFeNiMn		-	Laser	P = 880 W; v = 10 mm/s; u = 8.6 g/min	-	[97]
CoCrFeNiMn		-	Laser	P = 350–400 W; v = 400–600 mm/min; L = 0.25–0.3 mm	FCC	[83]
CoCrFeNiMo		-	Laser	P = 950 W; v = 250 mm/min; L = 0.3 mm; u = 9.5 g/min	FCC + σ + μ phase	[79]
CoCrFeNiMo <sub>0.2</sub>		-	Laser	P = 1000–1400 W; v = 400 mm/min; L = 0.25 mm	FCC	[98]
CoCrFeNiMo <sub>0.2</sub>		-	Laser	P = 1000–1400 W; u = 7–9 g/min; L = 0.25 mm	FCC	[85]
CoCrFeNiNbx (x = 0, 0.1, 0.15, 0.2)		-	Laser	P = 1600–1650 W; v = 7 mm/s	FCC (x = 0, 0.1 and 0.15); FCC + Laves (x = 0.2);	[99]
CoCrFeNiW <sub>x</sub> (x = 0, 0.2, 0.5, 0.7, and 1.0)		DML-V03AD	Plasma arc	v = 5 mm/s; P = 80 A; L = 3 mm	FCC (x = 0); FCC + μ phase (x = 2); FCC + BCC + μ phase (x = 7, 10)	[100]
CrMnFeCoNi		-	Laser	P = 1700 W; v = 2 mm/s; u = 10 g/min	FCC	[86]
CrMnFeCoNi		-	Laser	P = 1000–1400 W; v = 400 mm/min; L = 0.45 mm (single direction and dual direction)	FCC	[101]
CrMnFeCoNi		-	Laser	P = 1000 W; v = 800 mm/min	FCC	[87]
CrMnFeCoNi/x wt.% TiC (x = 0, 2.5 and 5)		-	Laser	-	FCC (x = 0); FCC + TiC (x = 2.5 and 5)	[102]
CrMnFeCoNi/x wt.% WC (x = 0, 5 and 10)		-	Laser	P = 1000 W; v = 500 mm/min	FCC (x = 0 and 5); FCC + M <sub>23</sub> C <sub>6</sub> (x = 10)	[103]
FeCrCoMnNi		-	Laser	P = 600–1000 W; v = 800 mm/min; L = 0.8 mm; u = 10 g/min	FCC	[104]

DED is utilized not only for fabricating large-scale HEA components, but also for the production of coatings. Numerous studies have attempted to utilize HEAs as a coating to clad on conventional alloys. Experimental data show that HEA coating can effectively improve the mechanical properties of samples, especially their wear resistance [46,96,105–108]. Moreover, DED is an efficient way to develop functionally graded HEAs, achieved using co-axial raw material feeders and each feeder's changeable powder flow rate [109–118]. Gwalani et al. [110] fabricated a compositionally graded HEA with a continuously altering chemical composition from Al<sub>0.3</sub>CoCrFeNi to Al<sub>0.7</sub>CoCrFeNi by loading two materials in two hoppers. In the beginning, Al<sub>0.3</sub>CoCrFeNi was deposited with specific layers. Then, the powder flow rate was gradually reduced to zero with the processing of DED and another hopper with Al<sub>0.7</sub>CoCrFeNi began to supply onto the previous sample. Figure 7a shows

the elemental composition change along the build direction of the sample. Figure 7b,c exhibit that three regions were formed in the graded HEA, as follows:  $Al_{0.3}CoCrFeNi$ , with only the FCC phase detected;  $Al_{0.7}CoCrFeNi$ , consisting of a dual phase of B2 + FCC; and the transition region results in the intermediate composition and complex microstructure consisting of elongated fcc grains, B2 precipitates along grain boundaries, and rudimentary lamellae of fcc and B2. The strength of the samples is efficiently adjusted by the FCC phase region (low hardness and strength), the B2 + FCC phase region (high hardness and strength), and the transition region. A DEDed  $Co_1Cr_1Cu_1Fe_1Ni_1Al_0$  to  $Co_1Cr_1Cu_1Fe_1Ni_1Al_3$  HEA was fabricated and investigated by Welk et al. [111]. A modulated plate-like microstructure is found in the matrix, a phase change at a given location across the plate-like phase is exhibited in Figure 8, and the phases enriching Cr, Fe, and Co were decomposed into Cr- and FeCo-rich domains, resulting from the spinodal decomposition of this disordered phase. The emergence of the graded HEA gives a new idea on the composition design of the AMed HEA alloy. The combination of varying phases with different properties through the transition area can complement each other.

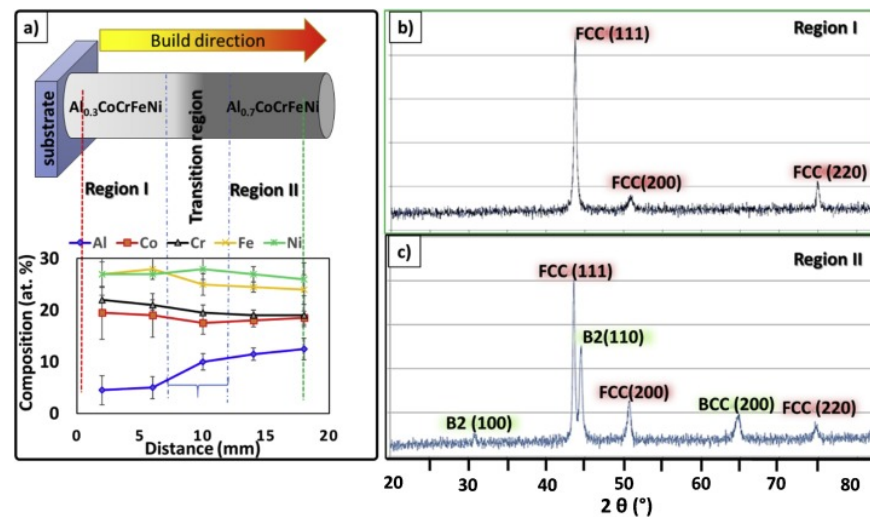


**Figure 7.** (a) Composition profile of the as-deposited  $Al_xCoCrFeNi$  graded laminate, (b) XRD patterns of  $Al_{0.3}CoCrFeNi$ , and (c)  $Al_{0.7}CoCrFeNi$  HEA, adapted with permission from Ref. [110]. Copyright of © 2024 Elsevier.

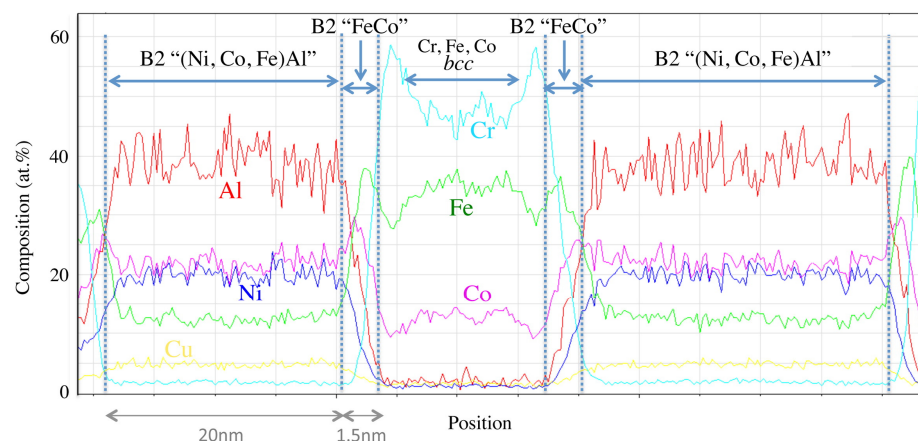


**Figure 8.** Elemental profile and corresponding phases at different locations of the  $Co_1Cr_1Cu_1Fe_1Ni_1Al_x$  HEA, adapted with permission from Ref. [111]. Copyright of © 2024 Elsevier.

### 3. The Design and Strengthening of CoCrFeNi-Based HEAs

The mechanical properties of HEAs are influenced by various factors, including the chemical composition, manufacturing procedures, and the resultant microstructure.

Given the typically low strength of CoCrFeNi HEA at room temperature, efforts have been made to enhance its performance by designing and developing CoCrFeNi-based HEAs. These CoCrFeNi-based HEAs typically possess superior strength and plasticity than CoCrFeNi HEAs.

Moreover, the rapid cooling rate in AM processes can lead to the refinement of grains and the introduction of a significant number of dislocations, hence enhancing the strength of CoCrFeNi-based HEAs. The approaches for enhancement based on the composition adjustment of CoCrFeNi can be classified into two types, as follows: the addition of element(s) with large or small atomic radii and the addition of micro or nanoparticles, as illustrated in Figure 9. In addition, appropriate post treatment after AM can further improve the mechanical properties of CoCrFeNi-based HEAs. It is also essential to probe the mechanical properties of the AMed HEAs to gain an in-depth understanding of the composition–microstructure–processing–properties relationships. In the following content, we discuss and summarize the tensile strength, ductility, the strength–ductility trade-off, and associated strengthening mechanisms based on the abovementioned categories.

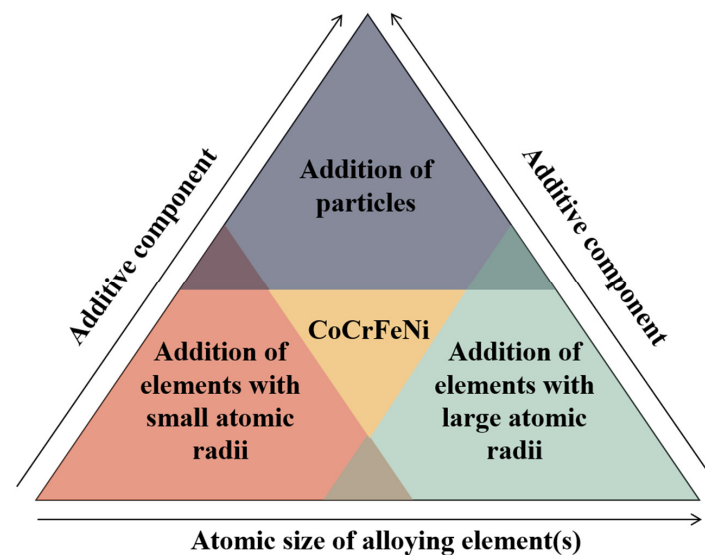


**Figure 9.** The transformation between CoCrFeNi- and CoCrFeNi-based HEAs based on the various additive types.

### 3.1. Addition of Element(s)

CoCrFeNiMn HEAs are one of the most widely studied HEAs, as a representative of HEAs crystallized into a single FCC solid solution. Excellent phase stability is observed for CoCrFeNiMn HEAs. The binary Gibbs energy–composition plots exhibit that all the binary systems in CoCrFeNiMn are FCC-promoting, apart from Cr–Mn. The Mn–Ni can compensate for the effect of Cr–Mn, with a considerably negative Gibbs energy for the FCC phase [119]. The strengthening effect brought about by the addition of Mn is negligible in the CoCrFeNi system, because the stresses caused by the lattice distortion are highly related to the deviations of atomic radius and shear modulus, which are very low for Mn compared to Cr, in the CoCrFeNiMn system [120].

AM processes usually generate hierarchical structures because of the different thermal histories along the depth of the sample. Dislocation cells have been found in the LPBFed CrMnFeCoNi sample, as shown in Figure 10 [121]. The dislocation wall was composed of tangled dislocations and multiple dislocations can be observed in the interiors of dislocation cells. Moreover, elemental segregation and twinned structures can also be found, making AM the promising way to fabricate parts with superior mechanical properties. Furthermore, deformation twinning can be observed and activated upon the plastic deformation of the AMed CoCrFeNiMn. It is known that the critical twinning stress for initiating deformation is negatively related to grain size. With the grain size increasing from 35.1  $\mu\text{m}$  to 88.9  $\mu\text{m}$ , the

deformation twinning stress increased from 542 MPa to 603 MPa [122]. The deformation twinning boundaries also act as barriers towards dislocation motion and interact with dislocations. In addition, the activation of the phase transformation from FCC to HCP was also identified among the AMed HEAs [121], a property which is also commonly found among low-SFE materials. Therefore, upon plastic deformation, the complex interactions between the dislocation–deformation and twinning–stacking faults contribute to the steady work-hardening capability and superior strength–ductility synergy.

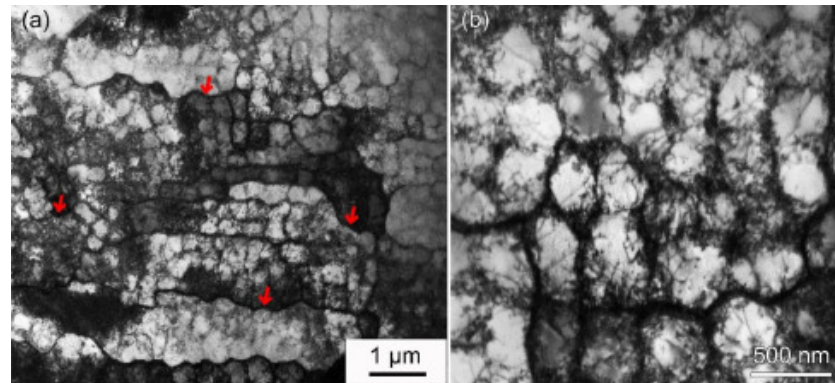


**Figure 10.** (a) TEM images showing cellular structure in the L-PBFed CrMnFeCoNi HEA. (b) A magnified image showing sub-micron cellular structures. The cell boundary was composed of tangled high-density dislocations (red arrows showing the grain boundaries), adapted with permission from Ref. [121]. Copyright of © 2024 Elsevier.

To enhance the solid solution strengthening and change the intrinsic mechanical properties in the FCC phase, various elements with different atomic radii are introduced into the FCC matrix to generate dual-phase structures to yield an improved strength [57,123,124]. Adding Al into the CoCrFeNi matrix is the most common way of increasing the strength and hardness of the matrix [40,93,95,125]. Al has been proven to promote the formation of BCC phases and inhibit the formation of FCC phases in HEAs, which can efficiently improve the strength of CoCrFeNi HEAs.

The addition of Al in CoCrFeNi alloys resulted in solid solution strengthening due to the large atomic radius of Al. The strength can be increased by more than ten times via alloying additions of Al. Joseph et al. [95] have manufactured  $Al_xCoCrFeNi$  ( $x = 0.3, 0.6,$  and  $0.85$ ) using DED and the results show that the tensile yield strength increases with the content of Al. The  $Al_{0.85}CoCrFeNi$  alloy samples possessed the highest yield strength of  $\sim 1400$  MPa and a ductility of 25%. The strength increment contributed to the phase transformation from a single FCC phase among the  $Al_{0.3}CoCrFeNi$  HEA to the spinodal decomposed BCC phase of the  $Al_{0.85}CoCrFeNi$  HEA. The large atomic size of Al generates solid solution strengthening, as well as precipitation hardening due to the spinodal-induced dense precipitates.

Some research is focused on the  $AlCoCrFeNi_{2.1}$  HEA, a type of eutectic HEA, possessing a “FCC + B2” lamellar microstructure, which shows an excellent combination of high tensile strength and ductility [40,57,92,126]. Ren et al. [40] have successfully fabricated  $AlCoCrFeNi_{2.1}$  HEA samples using LPBF. The dual-phase nanolamellar eutectic structure consists of an FCC phase and a BCC phase. Detailed microstructural characterizations into the BCC phase reveal the bicontinuous Ni–Al-rich and Co–Cr–Fe-rich nanostructures. Such nanolamellar structures are thought to be the primary reason for the high strength of LPBFed  $AlCoCrFeNi_{2.1}$  HEAs. Moreover, the high density of dislocation introduced using LPBF also contributes to improving strength, exceeding 1300 MPa.

Other alloy elements, such as W [100], Nb [99], Ti [62], Mo [69] and so on, have been studied to investigate the influence of phase evolution and microstructure on the mechanical properties. The tensile properties and strengthening mechanisms for AMed alloy element-enhanced CoCrFeNi-based alloys are summarized in Table 4.

**Table 4.** Tensile properties and related strengthening mechanisms of CoCrFeNi-based alloys (enhanced by alloy elements).

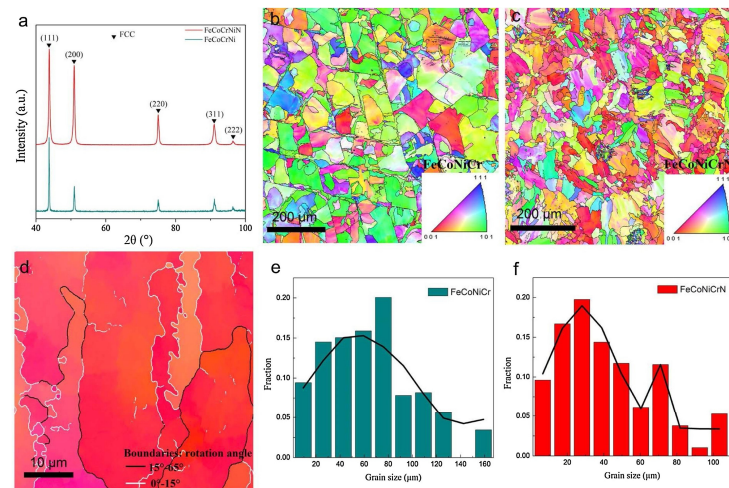
HEA Compositions	Manufacturing Process	Yield Strength (Mpa)	Ultimate Tensile Strength (Mpa)	Elongation (%)	Strengthening Mechanisms	Ref.
AlCoCrFeNi	EBM	769 ± 12.7 (BD 0°)	1073.5 ± 21.3 (BD 0°); 312.6 ± 114.5 (BD 90°)	1.2 ± 0.2 (BD 0°); 0 (BD 90°)	-	[78]
AlCoCrFeNi <sub>2,1</sub>	LPBF	1329	1621	11.7	Grain boundary strengthening and phase boundary strengthening within the nanolamellar structure and the high density of dislocation introduced using LPBF	[57]
AlCoCrFeNi <sub>2,1</sub>	DED	421.1 (top)/ 389.1 (bottom)	929.1 (top); 981.8 (bottom)	15.6 (top) 21 (bottom)	Second phase strengthening	[92]
AlCoCrFeNi <sub>2,1</sub>	LPBF	1333	1640	13.6	Interface strengthening and dislocation strengthening introduced using LPBF	[40]
Al <sub>0,3</sub> CoCrFeNi	LPBF	730	896	29%	High dislocation density caused by using LPBF, grain refinement and crystallographic texture	[54]
Al <sub>0,3</sub> CoCrFeNi	DED+Annealing	410; 500 (500 °C with 100 h); 630 (620 °C with 50 h)	-	28 (500 °C with 100 h); 18 (620 °C with 50 h)	Precipitation strengthening	[93]
Al <sub>0,3</sub> CoCrFeNi	DED	194	250	40	-	[125]
Al <sub>0,3</sub> Ti <sub>0,2</sub> Co <sub>0,7</sub> CrFeNi <sub>1,7</sub>	DED+Annealing	700; 1000 (800 °C with 5 h); 1150 (600 °C with 50 h)	1100; 1300 (800 °C with 5 h); 1420 (600 °C with 50 h)	18; 5 (800 °C with 5 h); 4.5 (600 °C with 50 h)	Precipitation strengthening	[94]
Al <sub>0,5</sub> CoCrFeNi	LPBF	609	878	18%	-	[60]
Al <sub>0,5</sub> FeCoCrNi	LPBF	579	721	22%	-	[58]
Al <sub>x</sub> CoCrFeNi	DED	200 (x = 0.3); 400 (x = 0.6); 1400 (x = 0.85);	1300 (x = 0.3); 1500 (x = 0.6); 220 (x = 0.85);	100 (x = 0.3); 78 (x = 0.6); 25 (x = 0.85);	Precipitation hardening and lattice distortion	[95]
Al <sub>x</sub> CoCrFeNi	LPBF	-	300 (x = 0); 520 (x = 0.1); 900 (x = 0.5)	12 (x = 0); 2 (x = 0.1); 10 (x = 0.5)	-	[53]
Co <sub>1,5</sub> CrFeNi <sub>1,5</sub> Ti <sub>0,5</sub> Mo <sub>0,1</sub>	LPBF+ST	773.0 ± 4.2	1178	25.8 ± 0.6%	Grain refinement	[62]
	EBM+ST	743.4 ± 11.6	932.2 ± 4.8	4.0 ± 0.2%	Ni <sub>3</sub> Ti intermetallic compounds for strengthening	
Co <sub>1,5</sub> CrFeNi <sub>1,5</sub> Ti <sub>0,5</sub> Mo <sub>0,1</sub>	EBM+ST	-	900; 1300 (ST-AC); 1100 (ST-WQ)	4; 18 (ST-AC); 37 (ST-WQ)	Homogeneous precipitation with ultrafine size	[77]

Table 4. Cont.

HEA Compositions	Manufacturing Process	Yield Strength (Mpa)	Ultimate Tensile Strength (Mpa)	Elongation (%)	Strengthening Mechanisms	Ref.
CoCrFeMnNi	LPBF	-	681	12.5	The reaction between Mn and oxygen reaction lead to what?	[38]
CoCrFeNiMn	LPBF+HT	465–510	541–609	19–34	Dislocation strengthening, friction stress, and grain boundary strengthening	[44]
CoCrFeNiMn	EBM	205 ± 3	497 ± 2	63 ± 1	-	[80]
CoCrFeNiMo <sub>0.2</sub>	DED	532 (P = 1000 W); 557 (P = 1200 W); 560 (P = 1400 W)	-	37 (P = 1000 W); 47 (P = 1200 W); 51 (P = 1400 W)	-	[98]
CoCrFeNiNbx (x = 0, 0.1, 0.15, 0.2)	DED	increase with the content of Nb		decrease with the content of Nb	The entanglement between the dislocations and the Laves phase	[99]
CoCrFeNiTiMo	LPBF	861 (BD 0°); 817 (BD 45°); 744 (BD 90°)	861 (BD 0°); 817 (BD 45°); 744 (BD 90°)	21 (BD 0°); 25 (BD 45°); 26 (BD 90°)	The anisotropic microstructure along BD and the existence of local strain	[69]
CoCrFeNiW <sub>x</sub>	DED	186.8 (x = 0); 284.8 (x = 0.2); 461.9 (x = 0.5); 554.5 (x = 0.7); 566.7 (x = 1)	526.6 (x = 0); 627.4 (x = 0.2); 786.8 (x = 0.5); 597.8 (x = 0.7); 566.7 (x = 1)	50.8 (x = 0); 28.7 (x = 0.2); 2.6 (x = 0.5); 0.6 (x = 0.7); 0.3 (x = 1)	Solid solution strengthening caused by W and second phase strengthening	[100]
CrMnFeCoNi	DED	353	564	26	Refined grain and high density of dislocation introduced using DED	[86]
CrMnFeCoNi	DED	517	660	26	The lattice friction resistance, fine grain strengthening, and dislocation strengthening	[127]
CrMnFeCoNi	DED	320.7; 427.4 (LSP = 1); 489.8 (LSP = 5)	531.7; 570.7 (LSP = 1); 639.9 (LSP = 5)	31.9; 40.1 (LSP = 1); 61 (LSP = 5)	LSP can improve the relative density of parts and accelerate grain refinement and the formation of nanotwins.	[87]
CoCrFeMnNi	LPBF+HIP	-	601; 649 (HIP)	35; 18 (HIP)	HIP can eliminate the micro-pore and micro-crack	[60]
CoCrFeNiMn	DED	518	660	19	Finer equiaxed grains and dendritic columnar grains and high density of dislocation introduced using DED	[97]
CoCrFeMnNi	DED+Annealing	424; 232.2 (annealed)	651.3; 647.1 (annealed)	47.9; 58.3 (annealed)	High dislocation density and fine cell structure	[83]

ST: solid solution; AC: air cooling; WQ: water quenching; HT: heat treatment; HIP: hot isostatic pressing; BD: building direction; LSP: laser shock peening.

Apart from alloy components, interstitial elements such as C, B, N, and others are commonly added to the CoCrFeNi-based matrix. These elements serve to reinforce the material by occupying interstitial positions within the host structure and generating nano-precipitates. Kim et al. [65] fabricated C-doped CoCrFeMnNi using LPBF and found that the formation of nanosized  $M_{23}C_6$ -type precipitates provided additional strengthening by interacting with dislocations and interrupting the crack propagation. The yield strength of the C-doped CoCrFeMnNi part can reach 800–900 MPa, with a maintained ductility of 25–30%. Seol et al. [128] added a small quantity of boron into  $Fe_{20}Mn_{20}Cr_{20}Co_{20}Ni_{20}$  and  $Fe_{40}Mn_{40}Cr_{10}Co_{10}$  HEAs. The results showed that all the doped HEAs have higher strength than their undoped counterparts and their ductility can also exceed the undoped sample with proper annealing treatment. It suggested that the small quantity of boron (300 ppm) can enhance the grain boundary cohesion and retard capillary-driven grain coarsening, which resulted in a reduced grain size. The dominant deformation mechanism in  $Fe_{20}Mn_{20}Cr_{20}Co_{20}Ni_{20}$  and  $Fe_{40}Mn_{40}Cr_{10}Co_{10}$  remained the same, twinning-induced plasticity (TWIP) and dislocation strain hardening and some mechanical twinning, leading to the improvement of strength and ductility. Zhang et al. [129] fabricated a NiCoFeCrAl<sub>3</sub> coating mixed with a small amount of C, Si, Mn, and Mo using laser cladding to enhance the solid solution strengthening, which is attributed to the atomic size mismatch. The microhardness increased from 506 HV (fabricated via arc melting) to 800 HV. The strength and ductility synergy can be achieved using AMed N-doped FeCoNiCr HEAs [64]. The hierarchically heterogeneous structures (Figure 11) comprised a bimodal grain structure, low-angle boundaries, and dislocation networks. The high strength was attributed to the plastic strain gradient generated from the deformation in the grain with different sizes and the solution strengthening from N atoms. The ductility was caused by the strain hardening from high back stress. Similar research on heterogeneous structures generated by introducing interstitial elements has been conducted by other researchers. In a previous study [130], adding C and N into FeCoCrNi exhibited heterogeneous structures consisting of fine grains distributed around coarse grains, a majority of high-angle GBs, a minority of low-angle GBs, and dislocation cell structures. The formation of such a structure can be promoted by introducing interstitial elements in the AMed HEAs, because overlapping the laser beam leads to re-melting in some regions where grains are refined more times than in others. In another study [131], LPBF manufactured, N-doped CoCrFeNi and the same heterogeneous structures were found, which provide effective diffusion paths to significantly promote the outward segregation of Cr, forming a thick protective Cr oxide layer, which renders excellent corrosion resistance. In Zhu's review [132], heterogeneous structures' extraordinary combination of strength and ductility are attributed to hetero-deformation-induced strengthening and hetero-deformation-induced strain hardening, separately. Both result from back and forward stress simultaneously, which are induced by a geometrically necessary dislocation pile-up. The effect of grain refinement, precipitate hardening, and dislocation hardening contributes to their superior tensile strength. Besides the effect of the doped interstitial elements, the rapid repeated thermal cycle of AM processes inhibits grain growth. Furthermore, it enhances the strength of the matrix via the Hall–Petch relationship. The processing parameters have an essential effect on deciding the grain size. Zhou et al. [42] manufactured CoCrFeNi and  $FeCoCrNiC_{0.05}$  HEAs with various laser parameters using LPBF. Figure 12 illustrates that the grain size decreased with the decreased laser power and the increased scanning speed. The selected laser parameters are critical because too high or low an energy density input produces intrinsic defects in the samples. The yield strength and elongation of interstitial element-doped AMed CoCrFeNi-based HEAs are summarized in Figure 13 and compared with the value of CoCrFeNi manufactured using AM and casting.



**Figure 11.** (a) XRD results, (b,c) EBSD IPF maps of undoped and N-doped FeCoNiCr. (d) The co-existence of both high-angle boundaries and low-angle boundaries in the N-doped FeCoNiCr. (e,f) Grain size distribution of undoped and N-doped HEAs, respectively, adapted with permission from Ref. [64]. Copyright of © 2024 Elsevier.

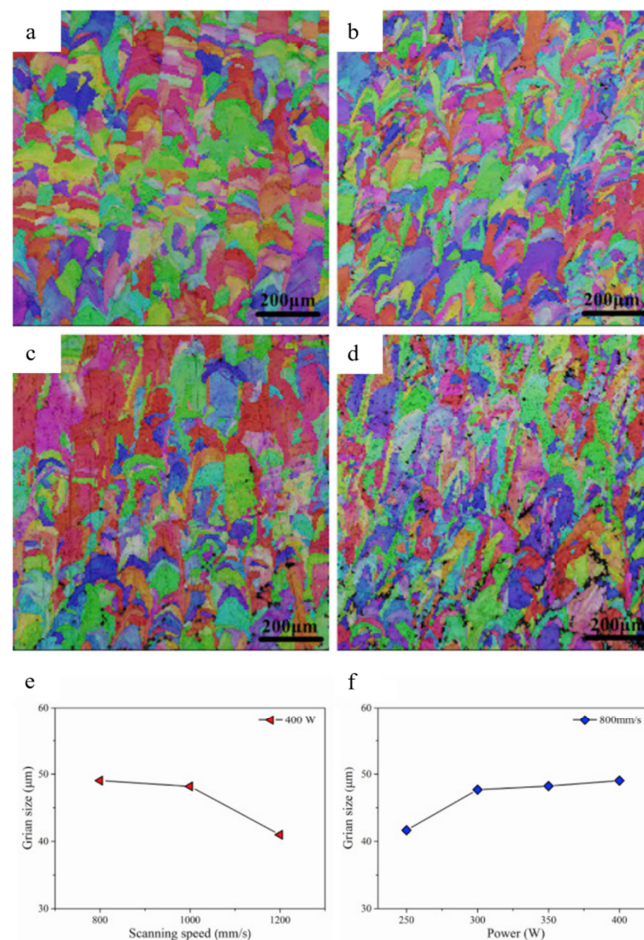


**Figure 12.** FeCoCrNiC<sub>0.05</sub> HEAs manufactured using LPBF with (a) 400 W, 800 mm/s; (b) 400 W, 1200 mm/s; (c) 300 W, 800 mm/s; and (d) 250 W, 800 mm/s. The evolution of grain size with (e) scanning speed and (f) laser power, adapted with permission from Ref. [42]. Copyright of © 2024 Elsevier.

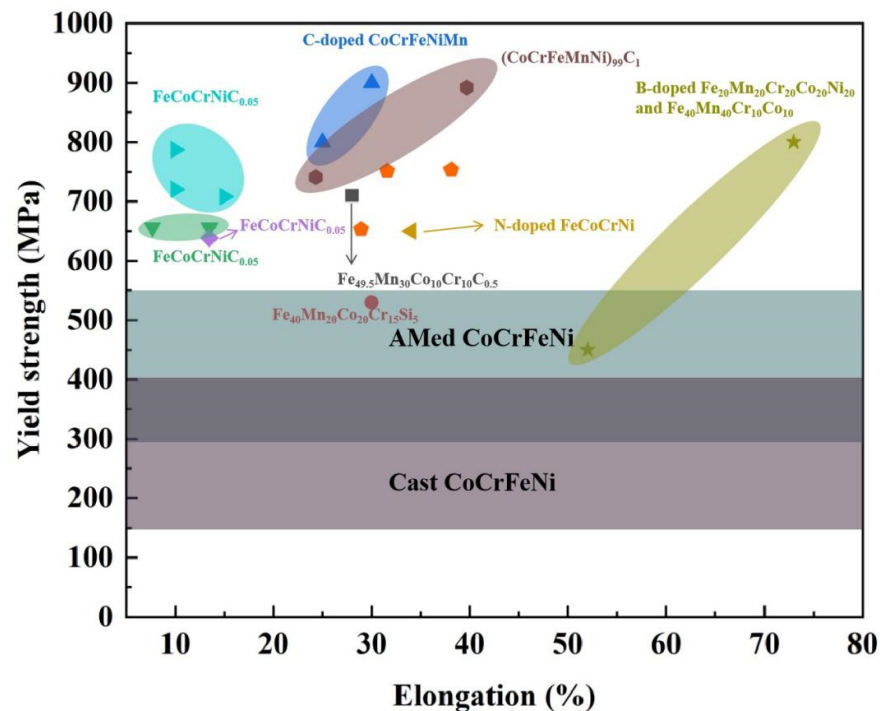


**Figure 13.** Summary of tensile yield strength versus elongation for interstitial element-doped AMed CoCrFeNi-based HEAs [41,42,64,65,70,128,133–136].

Upon plastic deformation, dislocations start to move and interact with each other, leading to an increase in the material's strength. This hardening effect can be illustrated by the strain hardening rate curve. There are typically three work-hardening stages for CoCrFeNi-based alloys [137–139]. The rapid strain-hardening rate drop in the first stage is due to the elastic–plastic transition during yielding, indicating that dislocation slip dominates the deformation. The plateau in the second stage indicates the activation of deformation twinning. Due to the significant back-stress [140] or an intersecting planar slip band, there may even be a steady increase in the second work-hardening stage [141]. At the third stage, the dislocation-accommodating capacity is running out, leading to a decreased work-hardening rate. Many factors jointly control the work hardening capacity, including temperature and strain rate [138], grain size, and the secondary phase in  $Al_xCoCrFeNi$  HEAs [142].

### 3.2. Additive of Micro/Nanoparticles

In addition to introducing alloy elements and interstitial elements to strengthen the matrix, micro or nanoparticles are added to modify the microstructure and properties of the HEAs. Most of the selected particles are ceramic, such as carbide [102,103,143–145], nitride [67,68,146], and oxide [147,148]. Shen et al. [143] have investigated the effect of the addition of SiC to the DEDed CoCrFeNi matrix. It is shown that  $Cr_7C_3$  appears in the samples of  $CoCrFeNi(SiC)_{0.3}$  and  $CoCrFeNi(SiC)_{0.5}$  HEAs, beside the FCC phase. The hardness and compressive strength increase with the increase in SiC, accompanied by the sacrifice of plasticity. The improvement is ascribed to the formation of  $Cr_7C_3$ . Moreover, the result of elemental distribution illustrates that a significant number of Si and a tiny amount of C were dissolved in the FCC phase, which caused the decrease in lattice parameters and enhanced the solid solution strengthening. Similarly, Amar et al. [102] fabricated a CrMnFeCoNi alloy with different TiC additions, using DED. It was found that the resulting tensile strength increased from 550 MPa for CrMnFeCoNi HEAs to 610 MPa for CrMnFeCoNi HEAs with 2.5 wt.% TiC and 723 MPa for CrMnFeCoNi HEAs with 5 wt.% TiC. The observation of the fracture surface of each sample shows that with the increase in TiC, the size of the dimple decreased until it vanished in the CrMnFeCoNi with 5 wt.%

TiC sample (Figure 14). The incorporation of TiC in the HEA resulted in a decrease in the number of slip bands, hence enhancing the strength of the material, while simultaneously reducing its plasticity. CrMnFeCoNi-based composites with a 0%, 5%, and 10% addition of WC were successfully manufactured using DED [103]. The grain size exhibited a reduction when the WC ratio increased (Figure 15a–c), whereas the  $\text{Cr}_{23}\text{C}_6$  precipitates were evenly distributed throughout the matrix (Figure 15d–g). The addition of WC can enhance the strength, resulting in a maximum yield strength of 675 MPa with a 10% WC content, compared to 300 MPa without WC. Nevertheless, the improvement in strength comes at the cost of reduced ductility, which declined from 50% to 9% due to the inclusion of WC. Incorporation of 5% WC contributes to the significant strength elevation from 300 MPa to 502 MPa without compromising too much ductility (from 50% to 37%). Therefore, these results demonstrated that the mechanical properties of HEAs can be tailored via carefully adjusting the phase fraction of the strengthener. Jiang et al. [147] conducted an investigation to examine the impact of  $\text{CeO}_2$  on the microstructure and characteristics of FeCoCrAlNiTi HEAs. They produced coatings of  $\text{CoCrAlNiTi}_x(\text{CeO}_2)$  ( $x = 0, 0.5, 1$  wt.%) via DED. The introduction of  $\text{CeO}_2$  resulted in the formation of dendritic structures that were consistently homogeneous and refined. The wear resistance is improved prominently and the wear mechanism changed from adhesive, oxidative, fatigue, and abrasive wear for the FeCoCrAlNiTi coating to mainly abrasive wear for the FeCoCrAlNiTi-1 wt.%  $\text{CeO}_2$  coating. The higher hardness and resistance to scratching and plastic deformation are ascribed to the refinement and solid solution strengthening caused by  $\text{CeO}_2$ . The addition of nitride to the HEA's matrix has a comparable effect to the inclusion of carbide or oxide in terms of changing the microstructure and mechanical characteristics. Resultingly, 5 wt.% TiN and 95 wt.% CoCrFeNiMn HEAs were successfully manufactured by Li et al. [67]. The printability is diminished by the addition of TiN, due to the augmentation of the laser reflectivity by the particles, necessitating a greater amount of energy to completely melt the powder mixture. An atomic diffusion occurs between the matrix and TiN and the matrix consisting of an FCC structure tends to be isotropic and equiaxial. The strength of the HEA composite is almost twice as much as that of the HEA. The primary factor contributing to this difference is the refinement, resulting from the rapid cooling rate in LPBF, coupled with the introduction of TiN as novel nucleation sites within the grain, which effectively suppresses grain development.

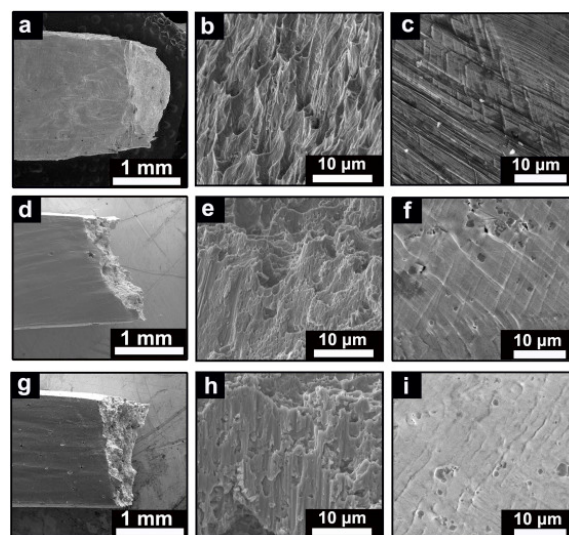


**Figure 14.** Observation of the fracture morphology of (a–c) CrMnFeCoNi HEAs, showing obvious necking and transgranular dimpled fractures; (d–f) CrMnFeCoNi HEAs with 2.5 wt.% TiC, showing shallow dimples on the fracture surface and a reduced number of slip bands; and (g–i) CrMnFeCoNi HEAs with 5 wt.% TiC, showing no dimple formations and associated brittle fractures, adapted with permission from Ref. [102]. Copyright of © 2024 Elsevier.

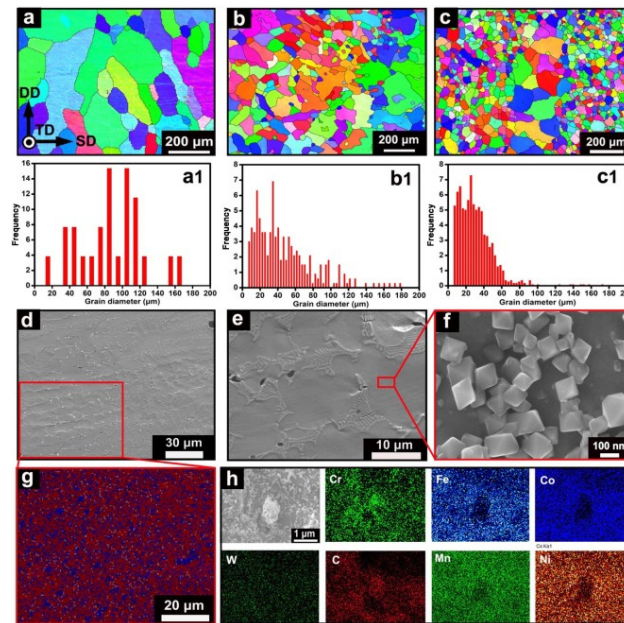


**Figure 15.** EBSD analysis and grain diameter distribution of CrMnFeCoNi HEAs with (a,a1) 0% WC, (b,b1) 5% WC, and (c,c1) 10% WC. (d–f) SEM images showing the formation of precipitates, (g) elemental partitioning behavior of the precipitate (blue color) and the matrix (red color), (h) elemental distribution between the precipitate and the matrix, adapted with permission from Ref. [103]. Copyright of © 2024 Elsevier.

A particular core–shell structure is sometimes mentioned in the research regarding AMed CoCrFeNi-based/particle HEAs. The reason for generating this structure is diverse. The core–shell structure was found in the LPBFed  $B_4C$ -added CoCrFeNi sample [144]. The structure was generated due to the  $B_4C$  not being fully melted, causing the carbide transformation in the precipitate. With a content of 1% wt.  $B_4C$ , the resulting tensile strength of CoCrFeNi/ $B_4C$  increased to 1421 MPa from 691.1 MPa for CoCrFeNi. The increased strength is mainly due to the formation of a core–shell structure (Figure 16), consisting of  $M_{23}C_6$ ,  $M_7C_3$ ,  $M_3C$  carbide, and  $Cr_2B$ . The transformation between varying carbides in the core–shell structure provides extra boundaries that can hinder and store the mobile dislocations and emit the stacking fault once the accumulated dislocation overpasses the critical stress. Egg-like core–shell structures were found to be formed in the  $Y_2O_3$ -doped AlCoCrCuFeNiSi<sub>0.5</sub> HEA [149].  $Y_2O_3$  functions as a catalyst that enhances the process of liquid phase separation. The core–shell was initially induced from the minority AlNi-rich liquid phase and transformed into a Cu-depleted phase (shell) and Cu-enriched phase (core), following the sequence of solidification. The tensile properties and strengthening mechanism for particle-enhanced CoCrFeNi-based HEAs are summarized in Table 5.

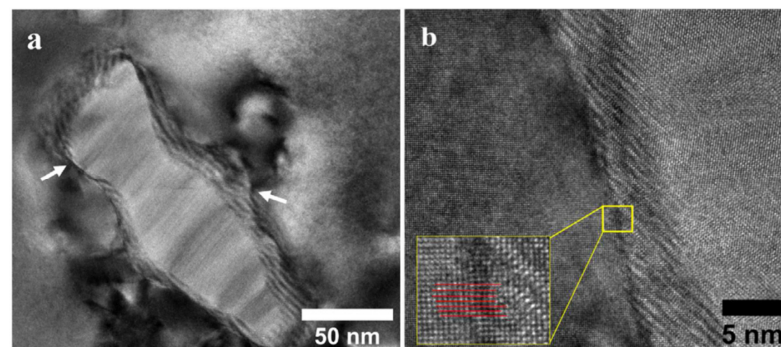


**Figure 16.** (a) The core–shell structure existing in the CoCrFeNi/ $B_4C$  HEA, (b) coherency between the matrix and the precipitate, adapted with permission from Ref. [144]. Copyright of © 2024 Elsevier.

**Table 5.** Tensile properties and related strengthening mechanisms of CoCrFeNi-based alloys (enhanced using micro/nanoparticles).

HEA Composition	Manufacturing Process	Yield Strength (Mpa)	Ultimate Tensile Strength (Mpa)	Elongation (%)	Strengthening Mechanisms	Ref.
(CoCrFeNi) <sub>100-x</sub> N <sub>x</sub> (x = 0, 0.25 and 0.50 at. %)	LPBF	530 (x = 0); 630 (x = 0.25); 730 (x = 0.5)	707 (x = 0); 807 (x = 0.25); 850 (x = 0.5)	43 (x = 0); 38 (x = 0.25); 29 (x = 0.5)	The interstitial strengthening caused by N	[146]
CoCrFeNi(SiC) <sub>x</sub> (x = 0, 0.1, 0.3 and 0.5)	DED	-	-	-	Second phase strengthening and solid solution strengthening.	[143]
CoCrFeNi-1 wt.% B <sub>4</sub> C	LPBF	1249.5	1421	10.60%	Hall-Petch strengthening, precipitate strengthening	[144]
CrMnFeCoNi-x wt.% TiC (x = 0, 0.25 and 0.5)	DED	300 (x = 0); 330 (x = 0.25); 385 (x = 0.5)	550 (x = 0); 610 (x = 0.25); 723 (x = 0.5)	50 (x = 0); 47 (x = 0.25); 32 (x = 0.5)	Dislocation movements are impeded by the addition of TiC	[102]
CoCrFeMnNi-5 wt.% NbC	LPBF+HT	870	1050	15	Grain refinement and dislocation strengthening	[145]
CoCrFeMnNi-12 wt.% TiN	LPBF	-	1100	7.5	The addition of TiN causes grain refinement.	[67]
CrMnFeCoNi-5 wt.% Fe <sub>54.5</sub> Cr <sub>18.4</sub> Mn <sub>2.0</sub> Mo <sub>13.9</sub> W <sub>5.8</sub> B <sub>3.2</sub> C <sub>0.9</sub> Si <sub>1.3</sub>	LPBF	675	820	12.3	Dislocation strengthening caused by the difference of thermal expansion coefficients between Fe-based metallic glass and matrix, solid solution strengthening, grain refinement strengthening, dispersion strengthening	[149]
FeCoCrNiMn-x wt.% Fe <sub>43.7</sub> Co <sub>7.3</sub> Cr <sub>14.7</sub> Mo <sub>12.6</sub> C <sub>15.5</sub> B <sub>4.3</sub> Y <sub>1.9</sub> (x = 5, 10, 20 and 30)	LPBF	315 (x = 0); 384 (x = 5); 595 (x = 10); 916 (x = 20)	-	80 (x = 5); 58 (x = 10); 39 (x = 20)	The solid solution strengthening caused by the atomic size mismatch between FeCoCrNiMn and the amorphous alloy and the resistance towards dislocation motion by the particle.	[63]
CrMnFeCoNi-x wt.% WC (x = 0, 5 and 10)	DED	300 (x = 0); 502 (x = 5); 675 (x = 10)	550 (x = 0); 776 (x = 5); 845 (x = 10)	50 (x = 0); 37 (x = 5); 9 (x = 10)	M <sub>23</sub> C <sub>6</sub> precipitates are formed, which hinder the propagation of slip bands, grain refinement, and precipitate strengthening.	[103]

HT: heat treatment.

#### 4. Post-Treatment Strategies for AMed HEAs

HEAs tend to become brittle following the AM process, due to the significant residual stress that is retained after rapid solidification. Heat treatment is commonly applied to AMed parts to relieve residual stress and enhance their properties and performance.

Annealing is one of the most popular heat treatments and it is commonly used in HEA studies [70,83,104,150–152]. Generally, the microstructure of the HEA can be tailored by the annealing treatment using the decomposition of the dislocation network and associated recrystallization under certain circumstances. Post-heat treatment of the AMed component might result in the formation of different forms of precipitates, depending on the matrix compositions and annealing temperatures. Lin et al. [150] have manufactured FeCoCrNi HEAs using LPBF and have clarified the relationship between strength and annealing temperature in the temperature range between 773 K and 1573 K. The shape of the grain tended to be equiaxed with the increased annealing temperatures, as shown in Figure 17. The residual stress reduced with the annealing temperature, the dislocation density in the grain decreased gradually, and the annealing twins were generated during recrystallization. The synergistic effect of dislocation annihilation, recrystallization, and internal stress relief reduces tensile strength and increases ductility.

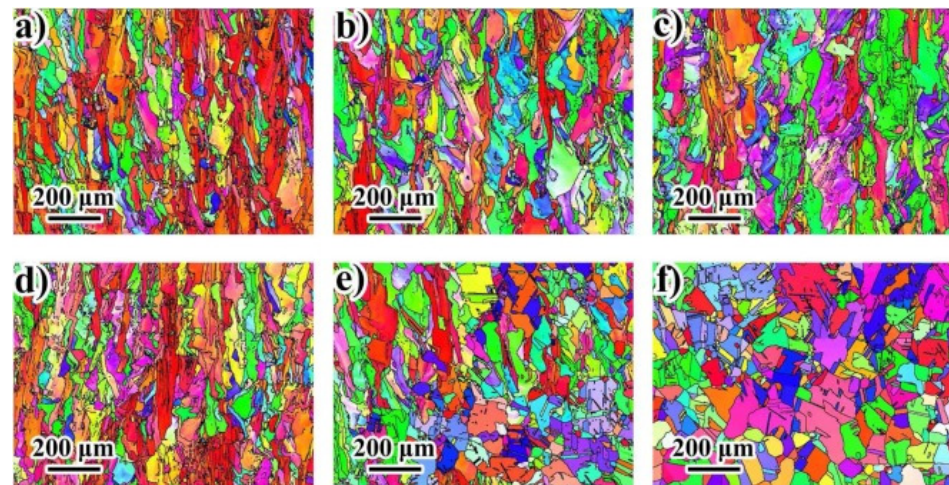


**Figure 17.** Grain structure of (a) the as-printed FeCoCrNi HEA sample; after 2 h of annealing at (b) 773 K, (c) 973 K, (d) 1173 K, (e) 1373 K, and (f) 1573 K, adapted with permission from Ref. [150]. Copyright of © 2024 Elsevier.

Solid solution heat treatment and aging heat treatment have also been used to adjust the mechanical properties of as-built parts [40,62,77,153,154]. LPBF and EBM have been utilized to manufacture  $\text{Co}_{1.5}\text{CrFeNi}_{1.5}\text{Ti}_{0.5}\text{Mo}_{0.1}$  HEAs with a relative density higher than 99% [62]. The solid solution treatment with water quenching improved the tensile stress and ductility of LPBFed and EBMed samples. The post-treatment not only altered the grain size and morphology of the sample, but also changed the size and volume fraction of the ordered precipitates in the sample. Figure 18 depicts the correlation between the size and volume fraction of the ordered precipitates and the tensile strength, as well as the relationship between grain size and strength in  $\text{Co}_{1.5}\text{CrFeNi}_{1.5}\text{Ti}_{0.5}\text{Mo}_{0.1}$  HEAs. Moreover, eliminating the  $\text{Ni}_3\text{Ti}$  phase can also contribute to enhancing its mechanical performance, since the  $\text{Ni}_3\text{Ti}$  intermetallic was considered the source of crack initiation and propagation, leading to early permanent fracture.

Besides the typical heat treatments that can be applied to most metals and alloys, hot isostatic pressing (HIP) is a promising solution for AMed metals and alloys because the combination of high temperature and pressure can effectively eliminate the internal pores in the AMed samples. The inherent residual stress generated by the rapid cooling process can be relieved to a great extent. Joseph et al. [155] have manufactured an  $\text{Al}_{0.3}\text{CoCrFeNi}$

alloy using DED and the relative density can reach 99.4%. The value can be increased up to 99.5% after HIP and it was found that HIP efficiently removed the pores with a large diameter ( $>5 \mu\text{m}$ ). The  $\text{Al}_{0.6}\text{CoCrFeNi}$  and  $\text{Al}_{0.85}\text{CoCrFeNi}$  samples showed less ductility after HIP, due to the growth of the B2 precipitate and the appearance of  $\sigma$ -phase precipitates. The trend was similar for the LPBF process. The relative density of  $\text{CoCrFeMnNi}$  increased from 98.2% to 99.1% after HIP [60]. The residual stress decreased after HIP, due to the simultaneous application of high pressure and temperature and the preferential orientation changed from  $\langle 001 \rangle$  texture to random grain orientation, accompanied by the homogeneously distributed elements. The tensile strength increased from 601 MPa to 649 MPa after HIP with the sacrifice of ductility.

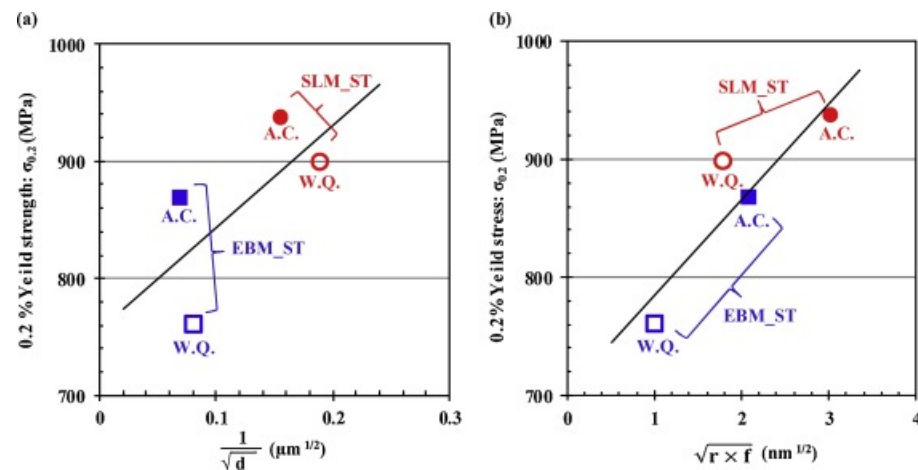


**Figure 18.** (a) Relationship between yield strength and grain size ( $d$ ) of solution-treated samples. (b) Dependence of radius of ordered precipitate ( $r$ ) and its volume fraction ( $f$ ) on yield strength of solution-treated samples, adapted with permission from Ref. [62]. Copyright of © 2024 Elsevier.

Other surface treatments, such as shot peening and ultrasonic impact treatment, are also used to minimize the residual stress of AMed metals and alloys. Laser shock peening (LSP) was implemented to modify the properties of  $\text{CrMnFeCoNi}$  HEAs manufactured using DED [87]. The LSP process was controlled by the laser energy input and the number of laser impacts. The surface roughness increased dramatically by increasing the impact number, because of the formation of craters. The residual stress on the surface of the sample tended to be compressive, due to the introduction of severe plastic deformations, which can remove the pores on the surface after manufacturing and improve the strength of the matrix. The generation and propagation of cracks were hindered by the compressive stress remaining on the surface during the tensile experiment, which caused concurrent increases in tensile stress and ductility. Most interestingly, the microstructure changed gradually along the thickness of the samples; the area close to the surface showed ultrafine grains and mechanical twins, while coarser grains and dislocations can be witnessed for those areas away from the free surface.

## 5. Summary and Perspective

HEAs have attracted considerable attention because of their unique characteristics that distinguish them from conventional metallic materials. Considerable efforts have been dedicated to investigating the possible utilization of HEAs, especially  $\text{CoCrFeNi}$ -based HEAs, in structural applications. From a compositional viewpoint,  $\text{CoCrFeNi}$ -based HEAs can be broadly classified into two groups. The first category involves incorporating one or more elements into the  $\text{CoCrFeNi}$ -based matrix. The elements can consist of alloy elements characterized by large atomic radii or interstitial elements distinguished by small atomic radii. The second category involves the incorporation of micro and nanoparticles into the  $\text{CoCrFeNi}$ -based alloy, mainly ceramic particles.

The implementation of the AM technique enhances the competitiveness and adaptability of the HEA community across many applications. Typically, the mechanical strength of AMed CoCrFeNi-based HEAs is higher than those produced using traditional methods, due to the rapid solidification observed in AM techniques. This might be attributed to the increased density of dislocations, resulting from the rapid solidification process. It is crucial to find out the optimal processing parameters of AM to achieve a high mechanical performance, and unsuitable parameters will bring in defects to the parts printed; for example, input energy can not only alter the grain size, but also introduce pores or cracks within the samples. Additionally, appropriate post-processing measures can further improve the mechanical properties of the AMed components, due to the elimination of deleterious phases and the reduction in residual stress. Usually, the LPBFed CoCrFeNi-based HEAs possess higher strength than the EBMed parts, because of the lower thermal gradient ratio to the melt pool's solidification rate. Nevertheless, LPBFed parts tend to have a higher internal stress than EBMed ones; the preheating procedure in EBM effectively mitigates the residual stress induced by the manufacturing process.

Most AMed CoCrFeNi-based HEAs exhibit single FCC phases. The most prevalent method for achieving an exceptional combination of strength and ductility in AMed CoCrFeNi-based HEAs is through the creation of the BCC phase inside the matrix by introducing BCC stabilizer elements or altering the adding element ratio. This is attributed to the inherent high strength of the BCC phases and ductility of the FCC phase. Additionally, processing temperatures such as energy input also greatly affect the phases formed. Increasing energy results in an elevated temperature in the molten pool; this effectively prevents the segregation of elements and the vaporization of elements with low melting points, leading to a phase discrepancy between the raw material and the prototypes. Furthermore, the utilization of lattice distortion and the formation of secondary precipitates also shows great potential in achieving enhanced mechanical characteristics.

Several strengthening mechanisms operate simultaneously at ambient temperature, broadly divided into solid solution strengthening, grain boundary strengthening, precipitate hardening, and dislocation hardening. When micro/nanoparticles are added to the matrix, the tiny particles will not only act as obstacles towards dislocation movement, but also become new nucleation sites in the grain, resulting in grain refinement. Interestingly, it has been shown that distinct core-shell structures can arise. Further study is required to confirm and explore the impact of the particle's core-shell structures on the mechanical properties of HEAs. Additionally, it expands the potential for future advancements in the design of compositions and the regulation of the mechanical properties of CoCrFeNi-based HEAs.

**Author Contributions:** Conceptualization, Z.W. and J.W.; methodology, Z.W.; Formal analysis, Z.W., S.W., Y.J., W.Z. and R.C.; resources, S.W. and Y.J.; data curation, W.Z. and R.C.; writing—original draft preparation, Z.W. and S.Y.; writing—review and editing, B.C., S.Y. and J.W.; project administration, S.Y. and J.W.; funding acquisition, B.C. and J.W. All authors have read and agreed to the published version of the manuscript.

**Funding:** The authors would like to acknowledge the financial support from the Shenzhen Science and Technology Program (Grant No. JCYJ20220818102403007, KQTD20200820113045083, KJZD20231023100000001, and GXWD20231129195215001), the National Natural Science Foundation of China (52201257 and 52301141), and the Shenzhen Research Fund for Returned Scholars (DD11409017).

**Data Availability Statement:** Not applicable.

**Conflicts of Interest:** The authors declare no conflicts of interest.

## References

1. Yeh, J.-W.; Chen, S.-K.; Lin, S.-J.; Gan, J.-Y.; Chin, T.-S.; Shun, T.-T.; Tsau, C.-H.; Chang, S.-Y. Nanostructured high-entropy alloys with multiple principal elements: Novel alloy design concepts and outcomes. *Adv. Eng. Mater.* **2004**, *6*, 299–303. [\[CrossRef\]](#)
2. Cantor, B.; Chang, I.T.H.; Knight, P.; Vincent, A.J.B. Microstructural development in equiatomic multicomponent alloys. *Mater. Sci. Eng. A* **2004**, *375*, 213–218. [\[CrossRef\]](#)
3. Zou, Y.; Okle, P.; Yu, H.; Sumigawa, T.; Kitamura, T.; Maiti, S.; Steurer, W.; Spolenak, R. Fracture properties of a refractory high-entropy alloy: In situ micro-cantilever and atom probe tomography studies. *Scr. Mater.* **2017**, *128*, 95–99. [\[CrossRef\]](#)
4. Roy, U.; Roy, H.; Daoud, H.; Glatzel, U.; Ray, K. Fracture toughness and fracture micromechanism in a cast AlCoCrCuFeNi high entropy alloy system. *Mater. Lett.* **2014**, *132*, 186–189. [\[CrossRef\]](#)
5. Chen, C.; Pang, S.J.; Cheng, Y.Y.; Zhang, T. Microstructure and mechanical properties of  $\text{Al}_{20-x}\text{Cr}_{20+0.5x}\text{Fe}_{20}\text{Co}_{20}\text{Ni}_{20+0.5x}$  high entropy alloys. *J. Alloys Compd.* **2016**, *659*, 279–287. [\[CrossRef\]](#)
6. He, J.Y.; Liu, W.H.; Wang, H.; Wu, Y.; Liu, X.J.; Nieh, T.G.; Lu, Z.P. Effects of Al addition on structural evolution and tensile properties of the FeCoNiCrMn high-entropy alloy system. *Acta Mater.* **2014**, *62*, 105–113. [\[CrossRef\]](#)
7. Hong, S.I.; Moon, J.; Hong, S.K.; Kim, H.S. Thermally activated deformation and the rate controlling mechanism in CoCrFeMnNi high entropy alloy. *Mater. Sci. Eng. A* **2017**, *682*, 569–576. [\[CrossRef\]](#)
8. Wang, C.; Li, T.H.; Liao, Y.C.; Li, C.L.; Jang, J.S.C.; Hsueh, C.H. Hardness and strength enhancements of CoCrFeMnNi high-entropy alloy with Nd doping. *Mater. Sci. Eng. A* **2019**, *764*, 138192. [\[CrossRef\]](#)
9. Kumar, N.; Li, C.; Leonard, K.J.; Bei, H.; Zinkle, S.J. Microstructural stability and mechanical behavior of FeNiMnCr high entropy alloy under ion irradiation. *Acta Mater.* **2016**, *113*, 230–244. [\[CrossRef\]](#)
10. Yang, T.F.; Xia, S.Q.; Guo, W.; Hu, R.; Poplawsky, J.D.; Sha, G.; Fang, Y.; Yan, Z.F.; Wang, C.X.; Li, C.Y.; et al. Effects of temperature on the irradiation responses of  $\text{Al}_{0.1}\text{CoCrFeNi}$  high entropy alloy. *Scr. Mater.* **2018**, *144*, 31–35. [\[CrossRef\]](#)
11. Gu, L.; Liang, N.N.; Liu, Y.; Chen, Y.Y.; Liu, J.H.; Sun, Y.X.; Zhao, Y.H. Novel as-cast NiAlCoFeNb dual-phase high-entropy alloys with high hardness. *Mater. Lett.* **2022**, *324*, 132676. [\[CrossRef\]](#)
12. Schuh, B.; Mendez-Martin, F.; Völker, B.; George, E.P.; Clemens, H.; Pippin, R.; Hohenwarter, A. Mechanical properties, microstructure and thermal stability of a nanocrystalline CoCrFeMnNi high-entropy alloy after severe plastic deformation. *Acta Mater.* **2015**, *96*, 258–268. [\[CrossRef\]](#)
13. Xie, J.; Dong, H.; Hao, Y.; Fan, Z.; Wang, C.A. Exploring the Formation Mechanism of Deformation Twins in CrMnFeCoNi High Entropy Alloy. *Acta Metall. Sin. (Engl. Lett.)* **2022**, *35*, 1275–1280. [\[CrossRef\]](#)
14. Feng, S.; Guan, S.; Story, W.A.; Ren, J.; Zhang, S.; Te, A.; Gleason, M.A.; Heelan, J.; Walde, C.; Birt, A.; et al. Cold Spray Additive Manufacturing of CoCrFeNiMn High-Entropy Alloy: Process Development, Microstructure, and Mechanical Properties. *J. Therm. Spray Technol.* **2022**, *42*, 720–734. [\[CrossRef\]](#)
15. Zhang, J.; Yan, Y.; Li, B. Selective Laser Melting (SLM) Additively Manufactured CoCrFeNiMn High-Entropy Alloy: Process Optimization, Microscale Mechanical Mechanism, and High-Cycle Fatigue Behavior. *Materials* **2022**, *15*, 8560. [\[CrossRef\]](#) [\[PubMed\]](#)
16. Zou, Y.; Li, S.; Li, Y. Revealing the deformation mechanisms of the heterogeneous structured CrMnFeCoNi high entropy alloy with ameliorated mechanical and corrosion resistance properties. *Surf. Coat. Technol.* **2022**, *441*, 128558. [\[CrossRef\]](#)
17. Qiao, Y.; Chen, Y.; Cao, F.H.; Wang, H.Y.; Dai, L.H. Dynamic behavior of CrMnFeCoNi high-entropy alloy in impact tension. *Int. J. Impact Eng.* **2021**, *158*, 104008. [\[CrossRef\]](#)
18. Wagner, C.; Laplanche, G. Effect of grain size on critical twinning stress and work hardening behavior in the equiatomic CrMnFeCoNi high-entropy alloy. *Int. J. Plast.* **2023**, *166*, 103651. [\[CrossRef\]](#)
19. Zhang, X.; Liu, L.; Yao, K.; Duan, K.; Wu, F.; Zhao, R.; Zhang, Y.; Shang, J.; Chen, M. The phase composition characteristics of AlCoCrFeNi high entropy alloy heat-treated by simple normalizing treatment and its effects on mechanical properties. *J. Alloys Compd.* **2022**, *926*, 166896. [\[CrossRef\]](#)
20. Castañeda, J.A.; Zambrano, O.A.; Alcázar, G.A.; Rodríguez, S.A.; Coronado, J.J. Stacking Fault Energy Determination in Fe-Mn-Al-C Austenitic Steels by X-ray Diffraction. *Metals* **2021**, *11*, 1701. [\[CrossRef\]](#)
21. Liu, S.F.; Wu, Y.; Wang, H.T.; Lin, W.T.; Shang, Y.Y.; Liu, J.B.; An, K.; Liu, X.J.; Wang, H.; Lu, Z.P. Transformation-reinforced high-entropy alloys with superior mechanical properties via tailoring stacking fault energy. *J. Alloys Compd.* **2019**, *792*, 444–455. [\[CrossRef\]](#)
22. Zhang, Y.H.; Zhuang, Y.; Hu, A.; Kai, J.J.; Liu, C.T. The origin of negative stacking fault energies and nano-twin formation in face-centered cubic high entropy alloys. *Scr. Mater.* **2017**, *130*, 96–99. [\[CrossRef\]](#)
23. Zheng, T.; Lv, J.; Wu, Y.; Wu, H.-H.; Liu, S.; Tang, J.; Zhou, M.; Wang, H.; Liu, X.; Jiang, S.; et al. Effects of stacking fault energy on the deformation behavior of CoNiCrFeMn high-entropy alloys: A molecular dynamics study. *Appl. Phys. Lett.* **2021**, *119*, 201907. [\[CrossRef\]](#)
24. Zhang, X.; Dong, R.; Guo, Q.; Hou, H.; Zhao, Y. Predicting the stacking fault energy in FCC high-entropy alloys based on data-driven machine learning. *J. Mater. Res. Technol.* **2023**, *26*, 4813–4824. [\[CrossRef\]](#)
25. Xiao, J.; Wu, N.; Ojo, O.; Deng, C. Stacking fault and transformation-induced plasticity in nanocrystalline high-entropy alloys. *J. Mater. Res.* **2021**, *36*, 2705–2714. [\[CrossRef\]](#)
26. Ai, C.; He, F.; Guo, M.; Zhou, J.; Wang, Z.J.; Yuan, Z.W.; Guo, Y.J.; Liu, Y.L.; Liu, L. Alloy design, micromechanical and macromechanical properties of CoCrFeNiTax eutectic high entropy alloys. *J. Alloys Compd.* **2018**, *735*, 2653–2662. [\[CrossRef\]](#)

27. Niu, Z.Z.; Xu, J.; Wang, T.; Wang, N.R.; Han, Z.H.; Wang, Y. Microstructure, mechanical properties and corrosion resistance of CoCrFeNiW<sub>x</sub> ( $x = 0, 0.2, 0.5$ ) high entropy alloys. *Intermetallics* **2019**, *112*, 106550. [[CrossRef](#)]
28. Jiang, H.; Jiang, L.; Qiao, D.X.; Lu, Y.P.; Wang, T.M.; Cao, Z.Q.; Li, T.J. Effect of Niobium on Microstructure and Properties of the CoCrFeNb<sub>x</sub>Ni High Entropy Alloys. *J. Mater. Sci. Technol.* **2017**, *33*, 712–717. [[CrossRef](#)]
29. Niu, Z.Z.; Wang, Y.Z.; Geng, C.; Xu, J.; Wang, Y. Microstructural evolution, mechanical and corrosion behaviors of as-annealed CoCrFeNiMox ( $x = 0, 0.2, 0.5, 0.8, 1$ ) high entropy alloys. *J. Alloys Compd.* **2020**, *820*, 153273. [[CrossRef](#)]
30. Xu, Z.J.; Li, Z.T.; Tong, Y.; Zhang, W.D.; Wu, Z.G. Microstructural and mechanical behavior of a CoCrFeNiCu<sub>4</sub> non-equiatomic high entropy alloy. *J. Mater. Sci. Technol.* **2021**, *60*, 35–43. [[CrossRef](#)]
31. Lv, Y.K.; Hu, R.Y.; Yao, Z.H.; Chen, J.; Xu, D.P.; Liu, Y.; Fan, X.H. Cooling rate effect on microstructure and mechanical properties of Al<sub>x</sub>CoCrFeNi high entropy alloys. *Mater. Des.* **2017**, *132*, 392–399. [[CrossRef](#)]
32. Bandyopadhyay, A.; Traxel, K.D.; Lang, M.; Juhasz, M.; Eliaz, N.; Bose, S. Alloy design via additive manufacturing: Advantages, challenges, applications and perspectives. *Mater. Today* **2022**, *52*, 207–224. [[CrossRef](#)]
33. Frazier, W.E. Metal additive manufacturing: A review. *J. Mater. Eng. Perform.* **2014**, *23*, 1917–1928. [[CrossRef](#)]
34. Bandyopadhyay, A.; Zhang, Y.; Bose, S. Recent developments in metal additive manufacturing. *Curr. Opin. Chem. Eng.* **2020**, *28*, 96–104. [[CrossRef](#)] [[PubMed](#)]
35. George, E.P.; Raabe, D.; Ritchie, R.O. High-entropy alloys. *Nat. Rev. Mater.* **2019**, *4*, 515–534. [[CrossRef](#)]
36. Han, C.; Fang, Q.; Shi, Y.; Tor, S.B.; Chua, C.K.; Zhou, K. Recent Advances on High-Entropy Alloys for 3D Printing. *Adv. Mater.* **2020**, *32*, 1903855. [[CrossRef](#)] [[PubMed](#)]
37. Li, W.; Xie, D.; Li, D.; Zhang, Y.; Gao, Y.; Liaw, P.K. Mechanical behavior of high-entropy alloys. *Prog. Mater. Sci.* **2021**, *118*, 100777. [[CrossRef](#)]
38. Chen, P.; Li, S.; Zhou, Y.H.; Yan, M.; Attallah, M.M. Fabricating CoCrFeMnNi high entropy alloy via selective laser melting in-situ alloying. *J. Mater. Sci. Technol.* **2020**, *43*, 40–43. [[CrossRef](#)]
39. Niu, P.D.; Li, R.D.; Yuan, T.C.; Zhu, S.Y.; Chen, C.; Wang, M.B.; Huang, L. Microstructures and properties of an equimolar AlCoCrFeNi high entropy alloy printed by selective laser melting. *Intermetallics* **2019**, *104*, 24–32. [[CrossRef](#)]
40. Ren, J.; Zhang, Y.; Zhao, D.X.; Chen, Y.; Guan, S.; Liu, Y.F.; Liu, L.; Peng, S.Y.; Kong, F.Y.; Poplawsky, J.D.; et al. Strong yet ductile nanolamellar high-entropy alloys by additive. *Nature* **2022**, *608*, 62–68. [[CrossRef](#)]
41. Wu, W.Q.; Zhou, R.; Wei, B.Q.; Ni, S.; Liu, Y.; Song, M. Nanosized precipitates and dislocation networks reinforced C-containing CoCrFeNi high-entropy alloy fabricated by selective laser melting. *Mater. Charact.* **2018**, *144*, 605–610. [[CrossRef](#)]
42. Zhou, R.; Liu, Y.; Zhou, C.S.; Li, S.Q.; Wu, W.Q.; Song, M.; Liu, B.; Liang, X.P.; Liaw, P.K. Microstructures and mechanical properties of C-containing FeCoCrNi high entropy alloy fabricated by selective laser melting. *Intermetallics* **2018**, *94*, 165–171. [[CrossRef](#)]
43. Guo, J.; Goh, M.; Zhu, Z.G.; Lee, X.; Nai, M.L.S.; Wei, J. On the machining of selective laser melting CoCrFeMnNi high-entropy alloy. *Mater. Des.* **2018**, *153*, 211–220. [[CrossRef](#)]
44. Zhu, Z.G.; Nguyen, Q.B.; Ng, F.L.; An, X.H.; Liao, X.Z.; Liaw, P.K.; Nai, S.M.L.; Wei, J. Hierarchical microstructure and strengthening mechanisms of a CoCrFeNiMn high entropy alloy additively manufactured by selective laser melting. *Scr. Mater.* **2018**, *154*, 20–24. [[CrossRef](#)]
45. Zhang, C.; Chen, G.J.; Dai, P.Q. Evolution of the microstructure and properties of laser-clad FeCrNiCoB<sub>x</sub> high-entropy alloy coatings. *Mater. Sci. Technol.* **2016**, *32*, 1666–1672. [[CrossRef](#)]
46. Ocelik, V.; Janssen, N.; Smith, S.N.; De Hosson, J.T.M. Additive Manufacturing of High-Entropy Alloys by Laser Processing. *Jom* **2016**, *68*, 1810–1818. [[CrossRef](#)]
47. Cai, Z.B.; Jin, G.; Cui, X.F.; Liu, Z.; Zheng, W.; Li, Y.; Wang, L.Q. Synthesis and microstructure characterization of Ni-Cr-Co-Ti-V-Al high entropy alloy coating on Ti-6Al-4V substrate by laser surface alloying. *Mater. Charact.* **2016**, *120*, 229–233. [[CrossRef](#)]
48. Sing, S.L.; Yeong, W.Y. Laser powder bed fusion for metal additive manufacturing: Perspectives on recent developments. *Virtual Phys. Prototyp.* **2020**, *15*, 359–370. [[CrossRef](#)]
49. Oliveira, J.P.; LaLonde, A.D.; Ma, J. Processing parameters in laser powder bed fusion metal additive manufacturing. *Mater. Des.* **2020**, *193*, 108762. [[CrossRef](#)]
50. Kumar, P.; Farah, J.; Akram, J.; Teng, C.; Ginn, J.; Misra, M. Influence of laser processing parameters on porosity in Inconel 718 during additive manufacturing. *Int. J. Adv. Manuf. Technol.* **2019**, *103*, 1497–1507. [[CrossRef](#)]
51. Chattopadhyay, C.; Prasad, A.; Murty, B.S. Phase prediction in high entropy alloys—A kinetic approach. *Acta Mater.* **2018**, *153*, 214–225. [[CrossRef](#)]
52. Lee, K.S.; Bae, B.; Kang, J.H.; Lim, K.R.; Na, Y.S. Multi-phase refining of an AlCoCrFeNi high entropy alloy by hot compression. *Mater. Lett.* **2017**, *198*, 81–84. [[CrossRef](#)]
53. Sun, Z.J.; Tan, X.P.; Wang, C.C.; Descoins, M.; Manginck, D.; Tor, S.B.; Jägle, E.A.; Zaefferer, S.; Raabe, D. Reducing hot tearing by grain boundary segregation engineering in additive manufacturing: Example of an Al<sub>x</sub>CoCrFeNi high-entropy alloy. *Acta Mater.* **2021**, *204*, 116505. [[CrossRef](#)]
54. Peyrouzet, F.; Hachet, D.; Soulas, R.; Navone, C.; Godet, S.; Gorsse, S. Selective Laser Melting of Al<sub>0.3</sub>CoCrFeNi High-Entropy Alloy: Printability, Microstructure, and Mechanical Properties. *JOM* **2019**, *71*, 3443–3451. [[CrossRef](#)]
55. Sun, K.; Peng, W.X.; Yang, L.L.; Fang, L. Effect of SLM Processing Parameters on Microstructures and Mechanical Properties of Al<sub>0.5</sub>CoCrFeNi High Entropy Alloys. *Metals* **2020**, *10*, 292. [[CrossRef](#)]

56. Karlsson, D.; Marshal, A.; Johansson, F.; Schuisky, M.; Sahlberg, M.; Schneider, J.M.; Jansson, U. Elemental segregation in an AlCoCrFeNi high-entropy alloy—A comparison between selective laser melting and induction melting. *J. Alloys Compd.* **2019**, *784*, 195–203. [[CrossRef](#)]
57. Chen, X.S.; Kong, J.; Li, J.L.; Feng, S.; Li, H.; Wang, Q.P.; Liang, Y.Z.; Dong, K.W.; Yang, Y. High-strength AlCoCrFeNi<sub>2.1</sub> eutectic high entropy alloy with ultrafine lamella structure via additive manufacturing. *Mater. Sci. Eng. A* **2022**, *854*, 143816. [[CrossRef](#)]
58. Zhou, P.F.; Xiao, D.H.; Wu, Z.; Ou, X.Q. Al<sub>0.5</sub>FeCoCrNi high entropy alloy prepared by selective laser melting with gas-atomized pre-alloy powders. *Mater. Sci. Eng. A* **2019**, *73*, 86–89. [[CrossRef](#)]
59. Chen, P.; Yao, X.Y.; Attallah, M.M.; Yan, M. In-situ alloyed CoCrFeMnNi high entropy alloy: Microstructural development in laser powder bed fusion. *J. Mater. Sci. Technol.* **2022**, *123*, 123–135. [[CrossRef](#)]
60. Li, R.D.; Niu, P.D.; Yuan, T.C.; Cao, P.; Chen, C.; Zhou, K.C. Selective laser melting of an equiatomic CoCrFeMnNi high-entropy alloy: Processability, non-equilibrium microstructure and mechanical property. *J. Alloys Compd.* **2018**, *746*, 125–134. [[CrossRef](#)]
61. Lu, T.W.; Yao, N.; Chen, H.Y.; Sun, B.H.; Chen, X.Y.; Scudino, S.; Kosiba, K.; Zhang, X.C. Exceptional strength-ductility combination of additively manufactured high-entropy alloy matrix composites reinforced with TiC nanoparticles at room and cryogenic temperatures. *Addit. Manuf.* **2022**, *56*, 102918. [[CrossRef](#)]
62. Fujieda, T.; Chen, M.C.; Shiratori, H.; Kuwabara, K.; Yamanaka, K.; Koizumi, Y.; Chiba, A.; Watanabe, S. Mechanical and corrosion properties of CoCrFeNiTi-based high-entropy alloy additive manufactured using selective laser melting. *Addit. Manuf.* **2019**, *25*, 412–420. [[CrossRef](#)]
63. Li, N.; Wu, S.X.; Ouyang, D.; Zhang, J.J.; Liu, L. Fe-based metallic glass reinforced FeCoCrNiMn high entropy alloy through selective laser melting. *J. Alloys Compd.* **2020**, *822*, 153695. [[CrossRef](#)]
64. Song, M.; Zhou, R.; Gu, J.; Wang, Z.W.; Ni, S.; Liu, Y. Nitrogen induced heterogeneous structures overcome strength-ductility trade-off in an additively manufactured high-entropy alloy. *Appl. Mater. Today* **2020**, *18*, 100498. [[CrossRef](#)]
65. Kim, J.G.; Park, J.M.; Seol, J.B.; Choe, J.; Yu, J.H.; Yang, S.; Kim, H.S. Nano-scale solute heterogeneities in the ultrastrong selectively laser melted carbon-doped CoCrFeMnNi alloy. *Mater. Sci. Eng. A* **2020**, *773*, 138726. [[CrossRef](#)]
66. Chen, H.Y.; Lu, T.W.; Wang, Y.G.; Liu, Y.; Shi, T.Y.; Prashanth, K.G.; Kosiba, K. Laser additive manufacturing of nano-TiC particles reinforced CoCrFeMnNi high-entropy alloy matrix composites with high strength and ductility. *Mater. Sci. Eng. A* **2022**, *833*, 142512. [[CrossRef](#)]
67. Li, B.; Zhang, L.; Xu, Y.; Liu, Z.Y.; Qian, B.; Xuan, F.Z. Selective laser melting of CoCrFeNiMn high entropy alloy powder modified with nano-TiN particles for additive manufacturing and strength enhancement: Process, particle behavior and effects. *Powder Technol.* **2020**, *360*, 509–521. [[CrossRef](#)]
68. Li, B.; Qian, B.; Xu, Y.; Liu, Z.Y.; Xuan, F.Z. Fine-structured CoCrFeNiMn high-entropy alloy matrix composite with 12 wt% TiN particle reinforcements via selective laser melting assisted additive manufacturing. *Mater. Lett.* **2019**, *252*, 88–91. [[CrossRef](#)]
69. Ikeda, T.; Yonehara, M.; Ikeshoji, T.T.; Nobuki, T.; Hatate, M.; Kuwabara, K.; Otsubo, Y.; Kyogoku, H. Influences of Process Parameters on the Microstructure and Mechanical Properties of CoCrFeNiTi Based High-Entropy Alloy in a Laser Powder Bed Fusion Process. *Crystals* **2021**, *11*, 549. [[CrossRef](#)]
70. Zhou, R.; Liu, Y.; Liu, B.; Li, J.; Fang, Q.H. Precipitation behavior of selective laser melted FeCoCrNiC<sub>0.05</sub> high entropy alloy. *Intermetallics* **2019**, *106*, 20–25. [[CrossRef](#)]
71. Biamino, S.; Penna, A.; Ackelid, U.; Sabbadini, S.; Tassa, O.; Fino, P.; Pavese, M.; Gennaro, P.; Badini, C. Electron beam melting of Ti-48Al-2Cr-2Nb alloy: Microstructure and mechanical properties investigation. *Intermetallics* **2011**, *19*, 776–781. [[CrossRef](#)]
72. Zhao, X.L.; Li, S.J.; Zhang, M.; Liu, Y.D.; Sercombe, T.B.; Wang, S.G.; Hao, Y.L.; Yang, R.; Murr, L.E. Comparison of the microstructures and mechanical properties of Ti-6Al-4V fabricated by selective laser melting and electron beam melting. *Mater. Des.* **2016**, *95*, 21–31. [[CrossRef](#)]
73. Murr, L.E.; Quinones, S.A.; Gaytan, S.M.; Lopez, M.L.; Rodela, A.; Martinez, E.Y.; Hernandez, D.H.; Martinez, E.; Medina, F.; Wicker, R.B. Microstructure and mechanical behavior of Ti-6Al-4V produced by rapid-layer manufacturing, for biomedical applications. *J. Mech. Behav. Biomed. Mater.* **2009**, *2*, 20–32. [[CrossRef](#)] [[PubMed](#)]
74. Rafi, H.K.; Karthik, N.V.; Gong, H.J.; Starr, T.L.; Stucker, B.E. Microstructures and mechanical properties of Ti6Al4V parts fabricated by selective laser melting and electron beam melting. *J. Mater. Eng. Perform.* **2013**, *22*, 3872–3883. [[CrossRef](#)]
75. Fujieda, T.; Shiratori, H.; Kuwabara, K.; Kato, T.; Yamanaka, K.; Koizumi, Y.; Chiba, A. First demonstration of promising selective electron beam melting method for utilizing high-entropy alloys as engineering materials. *Mater. Lett.* **2015**, *159*, 12–15. [[CrossRef](#)]
76. Shiratori, H.; Fujieda, T.; Yamanaka, K.; Koizumi, Y.; Kuwabara, K.; Kato, T.; Chiba, A. Relationship between the microstructure and mechanical properties of an equiatomic AlCoCrFeNi high-entropy alloy fabricated by selective electron beam melting. *Mater. Sci. Eng. A* **2016**, *656*, 39–46. [[CrossRef](#)]
77. Fujieda, T.; Shiratori, H.; Kuwabara, K.; Hirota, M.; Kato, T.; Yamanaka, K.; Koizumi, Y.; Chiba, A.; Watanabe, S. CoCrFeNiTi-based high-entropy alloy with superior tensile strength and corrosion resistance achieved by a combination of additive manufacturing using selective electron beam melting and solution treatment. *Mater. Lett.* **2017**, *189*, 148–151. [[CrossRef](#)]
78. Kuwabara, K.; Shiratori, H.; Fujieda, T.; Yamanaka, K.; Koizumi, Y.; Chiba, A. Mechanical and corrosion properties of AlCoCrFeNi high-entropy alloy fabricated with selective electron beam melting. *Addit. Manuf.* **2018**, *23*, 264–271. [[CrossRef](#)]
79. Sui, Q.X.; Wang, Z.; Wang, J.; Xu, S.R.; Liu, B.; Yuan, Q.; Zhao, F.J.; Gong, L.; Liu, J. Additive manufacturing of CoCrFeNiMo eutectic high entropy alloy: Microstructure and mechanical properties. *J. Alloys Compd.* **2022**, *913*, 165239. [[CrossRef](#)]

80. Wang, P.; Huang, P.; Ng, F.L.; Sin, W.J.; Lu, S.; Nai ML, S.; Dong, Z.; Wei, J. Additively manufactured CoCrFeNiMn high-entropy alloy via pre-alloyed powder. *Mater. Des.* **2019**, *168*, 107576. [[CrossRef](#)]
81. Yamanaka, K.; Shiratori, H.; Mori, M.; Omura, K.; Fujieda, T.; Kuwabara, K.; Chiba, A. Corrosion mechanism of an equimolar AlCoCrFeNi high-entropy alloy additively manufactured by electron beam melting. *NPJ Mater. Degrad.* **2020**, *4*, 12. [[CrossRef](#)]
82. Herzog, D.; Seyda, V.; Wycisk, E.; Emmelmann, C. Additive manufacturing of metals. *Acta Mater.* **2016**, *117*, 371–392. [[CrossRef](#)]
83. Melia, M.A.; Carroll, J.D.; Whetten, S.R.; Esmaeely, S.N.; Locke, J.; White, E.; Anderson, I.; Chandross, M.; Michael, J.R.; Argibay, N.; et al. Mechanical and Corrosion Properties of Additively Manufactured CoCrFeMnNi High Entropy Alloy. *Addit. Manuf.* **2019**, *29*, 100833. [[CrossRef](#)]
84. Haase, C.; Tang, F.; Wilms, M.B.; Weisheit, A.; Hallstedt, B. Combining thermodynamic modeling and 3D printing of elemental powder blends for high-throughput investigation of high-entropy alloys—Towards rapid alloy screening and design. *Mater. Sci. Eng. A* **2017**, *688*, 180–189. [[CrossRef](#)]
85. Xiang, S.; Luan, H.W.; Wu, J.; Yao, K.F.; Li, J.F.; Liu, X.; Tian, Y.Z.; Mao, W.L.; Bai, H.; Le, G.M.; et al. Microstructures and mechanical properties of CrMnFeCoNi high entropy alloys fabricated using laser metal deposition technique. *J. Alloys Compd.* **2019**, *773*, 387–392. [[CrossRef](#)]
86. Qiu, Z.; Yao, C.; Feng, K.; Li, Z.; Chu, P.K. Cryogenic deformation mechanism of CrMnFeCoNi high-entropy alloy fabricated by laser additive manufacturing process. *Int. J. Lightweight Mater. Manuf.* **2018**, *1*, 33–39. [[CrossRef](#)]
87. Tong, Z.P.; Liu, H.L.; Jiao, J.F.; Zhou, W.F.; Yang, Y.; Ren, X.D. Improving the strength and ductility of laser directed energy deposited CrMnFeCoNi high-entropy alloy by laser shock peening. *Addit. Manuf.* **2020**, *35*, 101417. [[CrossRef](#)]
88. Gao, X.Y.; Lu, Y.Z. Laser 3D printing of CoCrFeMnNi high-entropy alloy. *Mater. Lett.* **2019**, *236*, 77–80. [[CrossRef](#)]
89. Wang, R.; Zhang, K.; Davies, C.; Wu, X.H. Evolution of microstructure, mechanical and corrosion properties of AlCoCrFeNi high-entropy alloy prepared by direct laser fabrication. *J. Alloys Compd.* **2017**, *694*, 971–981. [[CrossRef](#)]
90. Kuncic, I.; Polanski, M.; Karczewski, K.; Plocinski, T.; Kurzydowski, K.J. Microstructural characterisation of high-entropy alloy AlCoCrFeNi fabricated by laser engineered net shaping. *J. Alloys Compd.* **2015**, *648*, 751–758. [[CrossRef](#)]
91. Vikram, R.J.; Murty, B.S.; Fabijanic, D.; Suwas, S. Insights into micro-mechanical response and texture of the additively manufactured eutectic high entropy alloy AlCoCrFeNi<sub>2.1</sub>. *J. Alloys Compd.* **2020**, *827*, 154034. [[CrossRef](#)]
92. Shen, Q.K.; Xue, J.X.; Zheng, Z.H.; Yu, X.Y.; Ou, N. Effect of thermal cycling on the microstructure and mechanical properties of AlCoCrFeNi<sub>2.1</sub> high-entropy alloy fabricated using powder plasma arc additive manufacturing. *Mater. Lett.* **2022**, *325*, 132902. [[CrossRef](#)]
93. Nartu, M.; Alamd, T.; Dasari, S.; Mantri, S.A.; Gorse, S.; Siller, H.; Dahotre, N.; Banerjee, R. Enhanced tensile yield strength in laser additively manufactured Al<sub>0.3</sub>CoCrFeNi high entropy alloy. *Materialia* **2020**, *9*, 100522. [[CrossRef](#)]
94. Nartu, M.; Chesetti, A.; Sharma, A.; Mantri, S.A.; Dahotre, N.B.; Banerjee, R. Engineering heterogeneous microstructures in additively manufactured high entropy alloys for high strength and strain hardenability. *Mater. Sci. Eng. A* **2022**, *849*, 143505. [[CrossRef](#)]
95. Joseph, J.; Jarvis, T.; Wu, X.H.; Stanford, N.; Hodgson, P.; Fabijanic, D.M. Comparative study of the microstructures and mechanical properties of direct laser fabricated and arc-melted AlxCoCrFeNi high entropy alloys. *Mater. Sci. Eng. A* **2015**, *633*, 184–193. [[CrossRef](#)]
96. Cai, Z.B.; Wang, Y.D.; Cui, X.F.; Jin, G.; Li, Y.; Liu, Z.; Dong, M.L. Design and microstructure characterization of FeCoNiAlCu high-entropy alloy coating by plasma cladding: In comparison with thermodynamic calculation. *Surf. Coat. Technol.* **2017**, *330*, 163–169. [[CrossRef](#)]
97. Chew, Y.; Bi, G.J.; Zhu, Z.G.; Ng, F.L.; Weng, F.; Liu, S.B.; Nai SM, L.; Lee, B.Y. Microstructure and enhanced strength of laser aided additive manufactured CoCrFeNiMn high entropy alloy. *Mater. Sci. Eng. A* **2019**, *744*, 137–144. [[CrossRef](#)]
98. Wang, Q.; Amar, A.; Jiang, C.L.; Luan, H.W.; Zhao, S.F.; Zhang, H.; Le, G.M.; Liu, X.; Wang, X.Y.; Yang, X.S.; et al. CoCrFeNiMo<sub>0.2</sub> high entropy alloy by laser melting deposition: Prospective material for low temperature and corrosion resistant applications. *Intermetallics* **2020**, *119*, 1106727. [[CrossRef](#)]
99. Zhou, K.X.; Li, J.J.; Wang, L.L.; Yang, H.O.; Wang, Z.J.; Wang, J.C. Direct laser deposited bulk CoCrFeNiNbx high entropy alloys. *Intermetallics* **2019**, *114*, 106592. [[CrossRef](#)]
100. Shen, Q.K.; Xue, J.X.; Yu, X.Y.; Zheng, Z.H.; Ou, N. Powder plasma arc additive manufacturing of CoCrFeNiWx high-entropy alloys: Microstructure evolution and mechanical properties. *J. Alloys Compd.* **2022**, *922*, 166245. [[CrossRef](#)]
101. Xiang, S.; Li, J.F.; Luan, H.W.; Amar, A.; Lu, S.Y.; Li, K.; Zhang, L.; Liu, X.; Le, G.M.; Wang, X.Y.; et al. Effects of process parameters on microstructures and tensile properties of laser melting deposited CrMnFeCoNi high entropy alloys. *Mater. Sci. Eng. A* **2019**, *743*, 412–417. [[CrossRef](#)]
102. Amar, A.; Li, J.F.; Xiang, S.; Liu, X.; Zhou, Y.Z.; Le, G.M.; Wang, X.Y.; Qu, F.S.; Ma, S.Y.; Dong, W.M.; et al. Additive manufacturing of high-strength CrMnFeCoNi-based High Entropy Alloys with TiC addition. *Intermetallics* **2019**, *109*, 162–166. [[CrossRef](#)]
103. Li, J.F.; Xiang, S.; Luan, H.W.; Amar, A.; Liu, X.; Lu, S.Y.; Zeng, Y.Y.; Le, G.M.; Wang, X.Y.; Qu, F.S.; et al. Additive manufacturing of high-strength CrMnFeCoNi high-entropy alloys-based composites with WC addition. *J. Mater. Sci. Technol.* **2019**, *35*, 2430–2434. [[CrossRef](#)]
104. Tong, Z.P.; Ren, X.D.; Jiao, J.F.; Zhou, W.F.; Ren, Y.P.; Ye, Y.X.; Larson, E.A.; Gu, J.Y. Laser additive manufacturing of FeCrCoMnNi high-entropy alloy: Effect of heat treatment on microstructure, residual stress and mechanical property. *J. Alloys Compd.* **2019**, *78*, 1144–1159. [[CrossRef](#)]

105. Lin, Y.C.; Cho, Y.H. Elucidating the microstructure and wear behavior for multicomponent alloy clad layers by in situ synthesis. *Surf. Coat. Technol.* **2008**, *202*, 4666–4672. [[CrossRef](#)]
106. Lin, Y.C.; Cho, Y.H. Elucidating the microstructural and tribological characteristics of NiCrAlCoCu and NiCrAlCoMo multicomponent alloy clad layers synthesized in situ. *Surf. Coat. Technol.* **2009**, *203*, 1694–1701. [[CrossRef](#)]
107. Ye, F.X.; Yang, Y.; Lou, Z.; Feng, L.Z.; Guo, L.; Yu, J.X. Microstructure and wear resistance of TiC reinforced AlCoCrFeNi<sub>2.1</sub> eutectic high entropy alloy layer fabricated by micro-plasma cladding. *Mater. Lett.* **2021**, *284*, 128859. [[CrossRef](#)]
108. Chao, Q.; Guo, T.T.; Jarvis, T.; Wu, X.H.; Hodgson, P.; Fabijanic, D. Direct laser deposition cladding of Al<sub>x</sub>CoCrFeNi high entropy alloys on a high-temperature stainless steel. *Surf. Coat. Technol.* **2017**, *332*, 440–451. [[CrossRef](#)]
109. Dobbstein, H.; Gurevich, E.L.; George, E.P.; Ostendorf, A.; Laplanche, G. Laser metal deposition of compositionally graded TiZrNbTa refractory high-entropy alloys using elemental powder blends. *Addit. Manuf.* **2019**, *25*, 252–262. [[CrossRef](#)]
110. Gwalani, B.; Gangireddy, S.; Shukla, S.; Yannetta, C.J.; Valentin, S.G.; Mishra, R.S.; Banerjee, R. Compositionally graded high entropy alloy with a strong front and ductile back. *Mater. Today Commun.* **2019**, *20*, 100602. [[CrossRef](#)]
111. Welk, B.A.; Williams, R.E.; Viswanathan, G.B.; Gibson, M.A.; Liaw, P.K.; Fraser, H.L. Nature of the interfaces between the constituent phases in the high entropy alloy CoCrCuFeNiAl. *Ultramicroscopy* **2013**, *134*, 193–199. [[CrossRef](#)] [[PubMed](#)]
112. Borkar, T.; Gwalani, B.; Choudhuri, D.; Mikler, C.V.; Yannetta, C.J.; Chen, X.; Ramanujan, R.V.; Styles, M.J.; Gibson, M.A.; Banerjee, R. A combinatorial assessment of Al<sub>x</sub>CrCuFeNi<sub>2</sub> (0 < x < 1.5) complex concentrated alloys: Microstructure, microhardness, and magnetic properties. *Acta Mater.* **2016**, *116*, 63–76.
113. Gwalani, B.; Soni, V.; Waseem, O.A.; Mantri, S.A.; Banerjee, R. Laser additive manufacturing of compositionally graded AlCrFeMoV<sub>x</sub> (x = 0 to 1) high-entropy alloy system. *Opt. Laser Technol.* **2019**, *113*, 330–337. [[CrossRef](#)]
114. Pegues, J.W.; Melia, M.A.; Puckett, R.; Whetten, S.R.; Argibay, N.; Kustas, A.B. Exploring additive manufacturing as a high-throughput screening tool for multiphase high entropy alloys. *Addit. Manuf.* **2021**, *37*, 101598. [[CrossRef](#)]
115. Li, Z.M.; Ludwig, A.; Savan, A.; Springer, H.; Raabe, D. Combinatorial metallurgical synthesis and processing of high-entropy alloys. *J. Mater. Res.* **2018**, *33*, 3156–3169. [[CrossRef](#)]
116. Guan, S.; Ren, J.; Mooraj, S.; Liu, Y.F.; Feng, S.; Zhang, S.B.; Liu, J.; Fan, X.S.; Liaw, P.K.; Chen, W. Additive Manufacturing of High-Entropy Alloys: Microstructural Metastability and Mechanical Behavior. *J. Phase Equilib. Diffus.* **2021**, *42*, 748–771. [[CrossRef](#)]
117. Welk, B.A.; Gibson, M.A.; Fraser, H.L. A Combinatorial Approach to the Investigation of Metal Systems that Form Both Bulk Metallic Glasses and High Entropy Alloys. *JOM* **2016**, *68*, 1021–1026. [[CrossRef](#)]
118. Borkar, T.; Chaudhary, V.; Gwalani, B.; Choudhuri, D.; Mikler, C.V.; Soni, V.; Alam, T.; Ramanujan, R.V.; Banerjee, R. A Combinatorial Approach for Assessing the Magnetic Properties of High Entropy Alloys: Role of Cr in AlCo<sub>x</sub>Cr<sub>1-x</sub>FeNi. *Adv. Eng. Mater.* **2017**, *19*, 1700048. [[CrossRef](#)]
119. Vaidya, M.; Guruvidyathri, K.; Murty, B.S. Phase formation and thermal stability of CoCrFeNi and CoCrFeMnNi equiatomic high entropy alloys. *J. Alloys Compd.* **2019**, *774*, 856–864. [[CrossRef](#)]
120. Salishchev, G.A.; Tikhonovsky, M.A.; Shaysultanov, D.G.; Stepanov, N.D.; Kuznetsov, A.V.; Kolodiy, I.V.; Tortika, A.S.; Senkov, O.N. Effect of Mn and V on structure and mechanical properties of high-entropy alloys based on CoCrFeNi system. *J. Alloys Compd.* **2014**, *591*, 11–21. [[CrossRef](#)]
121. Wang, H.; Zhu, Z.G.; Chen, H.; Wang, A.G.; Liu, J.Q.; Liu, H.W.; Zheng, R.K.; Nai, S.M.; Primig, S.; Babu, S.S.; et al. Effect of cyclic rapid thermal loadings on the microstructural evolution of a CrMnFeCoNi high-entropy alloy manufactured by selective laser melting. *Acta Mater.* **2020**, *196*, 609–625. [[CrossRef](#)]
122. Sun, S.J.; Tian, Y.Z.; Lin, H.R.; Yang, H.J.; Dong, X.G.; Wang, Y.H.; Zhang, Z.F. Transition of twinning behavior in CoCrFeMnNi high entropy alloy with grain refinement. *Mater. Sci. Eng. A* **2018**, *712*, 603–607. [[CrossRef](#)]
123. Li, Z.M.; Tسان, C.C.; Pradeep, K.G.; Raabe, D. A TRIP-assisted dual-phase high-entropy alloy: Grain size and phase fraction effects on deformation behavior. *Acta Mater.* **2017**, *131*, 323–335. [[CrossRef](#)]
124. Nutor, R.K.; Cao, Q.P.; Wei, R.; Su, Q.M.; Du, G.H.; Wang, X.D.; Li, F.S.; Zhang, D.X.; Jiang, J.Z. A dual-phase alloy with ultrahigh strength-ductility synergy over a wide temperature range. *Sci. Adv.* **2021**, *7*, 4404. [[CrossRef](#)] [[PubMed](#)]
125. Joseph, J.; Stanford, N.; Hodgson, P.; Fabijanic, D.M. Tension/compression asymmetry in additive manufactured face centered cubic high entropy alloy. *Scr. Mater.* **2017**, *129*, 30–34. [[CrossRef](#)]
126. Huang, L.F.; Sun, Y.N.; Chen, N.; Luan, H.W.; Le, G.M.; Liu, X.; Ji, Y.Q.; Lu, Y.P.; Liaw, P.K.; Yang, X.S.; et al. Simultaneously enhanced strength-ductility of AlCoCrFeNi<sub>2.1</sub> eutectic high-entropy alloy via additive manufacturing. *Mater. Sci. Eng. A* **2022**, *830*, 142327. [[CrossRef](#)]
127. Guan, S.; Wan, D.; Solberg, K.; Berto, G.; Welo, T.; Yue, T.M.; Chan, K.C. Additive manufacturing of fine-grained and dislocation-populated CrMnFeCoNi high entropy alloy by laser engineered net shaping. *Mater. Sci. Eng. A* **2019**, *76*, 138056. [[CrossRef](#)]
128. Seol, J.B.; Bae, J.W.; Li, Z.M.; Han, J.C.; Kim, J.G.; Raabe, D.; Kim, H.S. Boron doped ultrastrong and ductile high-entropy alloys. *Acta Mater.* **2018**, *151*, 366–376. [[CrossRef](#)]
129. Zhang, H.; He, Y.Z.; Pan, Y.; He, Y.S.; Shin, K. Synthesis and characterization of NiCoFeCrAl<sub>3</sub> high entropy alloy coating by laser cladding. In Proceedings of the International Conference on Manufacturing Science and Engineering (ICMSE 2009), Zhuhai, China, 26–28 December 2009; Trans Tech Publications Ltd.: Stafa, Switzerland, 2009; pp. 1408–1411.

130. Chen, W.Y.; Zhou, R.; Li, W.P.; Chen, Y.H.; Chou, T.H.; Wang, X.; Liu, Y.; Zhu, Y.T.; Huang, J. Effect of interstitial carbon and nitrogen on corrosion of FeCoCrNi multi-principal element alloys made by selective laser melting. *J. Mater. Sci. Technol.* **2023**, *148*, 52–63. [[CrossRef](#)]
131. Zhou, R.; Chen, W.Y.; Li, W.P.; Chou, T.H.; Chen, Y.H.; Liang, X.P.; Luan, J.H.; Zhu, Y.T.; Huang, J.C.; Liu, Y. 3D printed N-doped CoCrFeNi high entropy alloy with more than doubled corrosion resistance in dilute sulphuric acid. *NPJ Mater. Degrad.* **2023**, *7*, 8. [[CrossRef](#)]
132. Zhu, Y.T.; Wu, X.L. Heterostructured materials. *Prog. Mater. Sci.* **2023**, *131*, 101019. [[CrossRef](#)]
133. Park, J.M.; Choe, J.; Kim, J.G.; Bae, J.W.; Moon, J.; Yang, S.; Kim, S.K.; Yu, J.H.; Kim, H.S. Superior tensile properties of 1%C-CoCrFeMnNi high-entropy alloy additively manufactured by selective laser melting. *Mater. Res. Lett.* **2020**, *8*, 1–7. [[CrossRef](#)]
134. Zhu, Z.G.; An, X.H.; Lu, W.J.; Li, Z.M.; Ng, F.L.; Liao, X.Z.; Ramamurty, U.; Nai, S.M.L.; Wei, J. Selective laser melting enabling the hierarchically heterogeneous microstructure and excellent mechanical properties in an interstitial solute strengthened high entropy alloy. *Mater. Res. Lett.* **2019**, *7*, 453–459. [[CrossRef](#)]
135. Agrawal, P.; Thapliyal, S.; Nene, S.S.; Mishra, R.S.; McWilliams, B.A.; Cho, K.C. Excellent strength-ductility synergy in metastable high entropy alloy by laser powder bed additive manufacturing. *Addit. Manuf.* **2020**, *32*, 101098. [[CrossRef](#)]
136. Kim, Y.K.; Yu, J.H.; Kim, H.S.; Lee, K.A. In-situ carbide-reinforced CoCrFeMnNi high-entropy alloy matrix nanocomposites manufactured by selective laser melting: Carbon content effects on microstructure, mechanical properties, and deformation mechanism. *Compos. Part B Eng.* **2021**, *210*, 108638. [[CrossRef](#)]
137. Gao, X.; Liu, T.; Qin, G.; Ren, H.; Zhou, Q.; Chen, R. Nano-twinning induced high strain hardening behavior in a metastable as-cast Co<sub>30</sub>Cr<sub>30</sub>Fe<sub>20</sub>Ni<sub>20</sub> high entropy alloy at room temperature. *Mater. Charact.* **2022**, *194*, 112420. [[CrossRef](#)]
138. Huang, G.; Li, B.; Chen, Y.; Xuan, F. Nanotwinning induced by tensile fatigue and dynamic impact of laser powder bed fusion additively manufactured CoCrFeNi high-entropy alloy. *J. Mater. Sci. Technol.* **2024**, *183*, 241–257. [[CrossRef](#)]
139. Rymer, L.M.; Frint, P.; Lindner, T.; Gebel, G.; Löbel, M.; Lampke, T. Strain-Rate Sensitive Deformation Behavior under Tension and Compression of Al<sub>0.3</sub>CrFeCoNiMo<sub>0.2</sub>. *Adv. Eng. Mater.* **2022**, *24*, 2100921. [[CrossRef](#)]
140. Li, J.; Yamanaka, K.; Chiba, A. Significant lattice-distortion effect on compressive deformation in Mo-added CoCrFeNi-based high-entropy alloys. *Mater. Sci. Eng. A* **2022**, *830*, 142295. [[CrossRef](#)]
141. Zhang, L.J.; Yu, P.F.; Fan, J.T.; Zhang, M.D.; Zhang, C.Z.; Cui, H.Z.; Li, G. Investigating the micro and nanomechanical properties of CoCrFeNi-C<sub>x</sub> high-entropy alloys containing eutectic carbides. *Mater. Sci. Eng. A* **2020**, *796*, 140065. [[CrossRef](#)]
142. Zhang, M.; Hou, J.; Yang, H.; Tan, Y.; Wang, X.; Shi, X.; Guo, R.; Qiao, J. Tensile strength prediction of dual-phase Al<sub>0.6</sub>CoCrFeNi high-entropy alloys. *Int. J. Min. Met. Mater.* **2020**, *27*, 1341. [[CrossRef](#)]
143. Shen, Q.K.; Kong, X.D.; Chen, X.Z.; Yao, X.K.; Deev, V.B.; Prusov, E.S. Powder plasma arc additive manufactured CoCrFeNi(SiC)<sub>x</sub> high-entropy alloys: Microstructure and mechanical properties. *Mater. Lett.* **2021**, *282*, 128736. [[CrossRef](#)]
144. Wu, Z.; He, M.; Cao, H.; Wang, S.; Chen, R.; Cao, B.; Shi, R.; Liu, X.; Yu, S.; Wang, S.; et al. Ultrahigh-strength and ductile CoCrFeNi-based high-entropy alloys manufactured by laser powder bed fusion with multiple strengthening mechanisms. *J. Mater. Res. Technol.* **2023**, *25*, 2948–2960. [[CrossRef](#)]
145. Li, R.X.; Kong, D.C.; He, K.T.; Dong, C.F. Superior thermal stability and strength of additively manufactured CoCrFeMnNi high-entropy alloy via NbC decorated sub-micro dislocation cells. *Scr. Mater.* **2023**, *230*, 115401. [[CrossRef](#)]
146. Zhang, Y.Y.; Ye, S.L.; Ke, H.B.; Chan, K.C.; Wang, W.H. In situ synthesis of N-containing CoCrFeNi high entropy alloys with enhanced properties fabricated by selective laser melting. *Mater. Des.* **2023**, *229*, 111891. [[CrossRef](#)]
147. Jiang, P.F.; Zhang, C.H.; Wu, C.L.; Zhang, S.; Zhang, J.B.; Abdullah, A.O. Microstructure and Properties of CeO<sub>2</sub>-Modified FeCoCrAlNiTi High-Entropy Alloy Coatings by Laser Surface Alloying. *J. Mater. Eng. Perform.* **2020**, *29*, 1346–1355. [[CrossRef](#)]
148. Zhang, H.; Wu, W.F.; He, Y.Z.; Li, M.X.; Guo, S. Formation of core-shell structure in high entropy alloy coating by laser cladding. *Appl. Surf. Sci.* **2016**, *363*, 543–547. [[CrossRef](#)]
149. Ma, Z.H.; Zhai, Q.; Wang, K.L.; Chen, G.X.; Yin, X.T.; Zhang, Q.X.; Meng, L.T.; Wang, S.H.; Wang, L. Fabrication of Fe-based metallic glass reinforced FeCoNiCrMn high-entropy alloy through additive manufacturing: Mechanical property enhancement and corrosion resistance improvement. *J. Mater. Res. Technol.* **2022**, *16*, 899–911. [[CrossRef](#)]
150. Lin, D.Y.; Xu, L.Y.; Jing, H.Y.; Han, Y.D.; Zhao, L.; Minami, F. Effects of annealing on the structure and mechanical properties of FeCoCrNi high-entropy alloy fabricated via selective laser melting. *Addit. Manuf.* **2020**, *32*, 101058. [[CrossRef](#)]
151. Duan, H.; Liu, B.; Fu, A.; He, J.Y.; Yang, T.; Liu, C.T.; Liu, Y. Segregation enabled outstanding combination of mechanical and corrosion properties in a FeCrNi medium entropy alloy manufactured by selective laser melting. *J. Mater. Sci. Technol.* **2022**, *99*, 207–214. [[CrossRef](#)]
152. Li, Z.; Zhao, P.C.; Lu, T.W.; Feng, K.; Tong, Y.G.; Sun, B.H.; Yao, N.; Xie, Y.; Han, B.L.; Zhang, X.C.; et al. Effects of post annealing on the microstructure, precipitation behavior, and mechanical property of a (CoCrNi)<sub>94</sub>Al<sub>3</sub>Ti<sub>3</sub> medium-entropy alloy fabricated by laser powder bed fusion. *J. Mater. Sci. Technol.* **2023**, *135*, 142–155. [[CrossRef](#)]
153. Mu, Y.K.; He, L.H.; Deng, S.H.; Jia, Y.F.; Jia, Y.D.; Wang, G.; Zhai, Q.J.; Liaw, P.K.; Liu, C.T. A high-entropy alloy with dislocation-precipitate skeleton for ultrastrength and ductility. *Acta Mater.* **2022**, *232*, 117975. [[CrossRef](#)]

154. Kuzminova, Y.O.; Firsov, D.G.; Dagesyan, S.A.; Konev, S.D.; Sergeev, S.N.; Zhilyaev, A.P.; Kawasaki, M.; Akhatov, I.S.; Evlashin, S.A. Fatigue behavior of additive manufactured CrFeCoNi medium-entropy alloy. *J. Alloys Compd.* **2021**, *863*, 158609. [[CrossRef](#)]
155. Joseph, J.; Hodgson, P.; Jarvis, T.; Wu, X.H.; Stanford, N.; Fabijanic, D.M. Effect of hot isostatic pressing on the microstructure and mechanical properties of additive manufactured AlxCoCrFeNi high entropy alloys. *Mater. Sci. Eng. A.* **2018**, *733*, 59–70. [[CrossRef](#)]

**Disclaimer/Publisher's Note:** The statements, opinions and data contained in all publications are solely those of the individual author(s) and contributor(s) and not of MDPI and/or the editor(s). MDPI and/or the editor(s) disclaim responsibility for any injury to people or property resulting from any ideas, methods, instructions or products referred to in the content.